

POLITECNICO DI TORINO

Corso di Laurea Magistrale in Ingegneria Energetica e Nucleare

Tesi di Laurea Magistrale

**Horizontal air-water two phase flow measurement
using Electrical Impedance Probes (SIET ECP and
DENERG ECP) and a Venturi Flow Meter (VFM)**



Relatori:

Prof. De Salve Mario

Prof. Bertani Cristina

**Candidato:
Giulia Chiesa**

Anno Accademico 2018/2019

Contents

Abstract	3
Sommario	4
1 Introduction	5
2 Two-phase flow	8
2.1 Models	8
2.2 Horizontal flow pattern classification	9
2.3 Definitions of variables used in two-phase flow	11
2.4 Flow pattern maps and transitions	14
2.4.1 Taitel and Dukler's map	14
2.5 Void fraction correlations	16
2.6 Spool Piece (SP)	17
2.6.1 Differential pressure meters	20
2.6.2 Impedance probes	24
3 Experimental facility, instrumentation	26
3.1 Test section	29
3.2 Instrumentation and signals acquisition	32
3.3 Spool Piece	35
3.3.1 Venturi Flow Meter VFM	35
3.3.2 SIET Electrical Capacitance Probe (SIET ECP)	39
3.3.3 DENERG Electrical Capacitance Probe (DENERG ECP)	43
4 Experimental campaign	45
4.1 Single-phase calibration	45
4.1.1 Calibration of the orifice and VFM	45
4.1.2 Calibration of ECPs	50
4.2 Experimental flow pattern with Taitel-Duckler map	60
4.3 Two-phase tests	61

<i>CONTENTS</i>	2
4.3.1 Analysis of VFM two-phase behaviour	76
4.3.2 Analysis of SIET ECP two-phase behavior	81
4.3.3 Analysis of the new DENERG ECP two-phase behavior	86
4.4 Combining signals: a general outline	89
5 Conclusions and perspectives	91
List of figures	92
List of tables	94
Bibliography	95

Abstract

Two-phase flow rate measurement is extremely important in many industrial sectors (nuclear, chemical, oil and gas, etc.). Nevertheless, the instrumentation required to perform these measurements is still very limited despite the huge research efforts of the last years. In the frame of the development of instrumentation for the two-phase flow rate measurement, the main aim of this study is the characterization of a Spool Piece (SP) consisting of a Venturi Flow Meter (VFM), and two Electric Capacitance Probes (ECPs) mounted in a horizontal test section, where an air-water two phase flow occurs. The measurements of differential pressures and electrical signals are analysed versus superficial velocities of liquid and gas, flow patterns and void fraction. The test section is a nominal ID 80 mm horizontal pipe with a Venturi Flow Meter (VFM), a new Electric Capacitance Probe with concave electrodes (DENERG ECP) and the Siet design of Electrical Capacitance Probe (SIET ECP) with ten long linear electrodes.

The flow rates in this experimental campaign are in the range of $0.048 - 0.0119 \text{ kg/s}$ for air (superficial velocity range 8-19 m/s) and $0 - 0.0535 \text{ kg/s}$ ($0 - 192 \text{ l/h}$) for water (superficial velocity range from 0.0006 m/s to 0.0103 m/s). These ranges of superficial velocities correspond to stratified-wavy and annular-dispersed flow patterns along the test section. This thesis work is divided into three main sections. The first one presents the description of the two-phase flow (models, classifications of flow patterns, definition of the main parameters and variables used, etc...), reasons why it is necessary to develop the so called Spool Piece (SP) constituted by several devices to measure two-phase parameters and a general overview on the differential pressure meters and impedance probes. In the second one the experimental facility, the test section, the instrumentation with their calibration and the method of acquisition of signals are described in detail. In the third section the experimental campaign with the experimental matrix and the test procedures to characterize the signals of VFM, the SIET ECP and the DENERG ECP. Finally, on the last subsection of the third section are estimate the total flow and the individual flow of the single phases based on the results of the present experimental campaign. In fact, the final goal is to combine the signals of the instruments to get the flow rate without the needing of the visual observation such as in the case of an opaque pipe.

Sommaro

La misurazione della portata bifase è estremamente importante in molti settori industriali (nucleare, chimico, petrolifero e del gas, ecc.). Nonostante gli enormi sforzi di ricerca degli ultimi anni, la strumentazione necessaria per eseguire queste misurazioni è ancora molto limitata. Nell'ambito dello sviluppo della strumentazione per la misurazione della portata bifase, l'obiettivo principale di questo studio è la caratterizzazione di uno Spool Piece (SP) costituito da un venturimetro (VFM) e da due sonde ad impedenza (ECPs) montato su una sezione di prova orizzontale, in cui si verifica un deflusso bifase aria-acqua. Vengono analizzate le cadute di pressione e i segnali elettrici rispetto alle velocità superficiali di liquido e gas, i regimi di flusso (flow patterns) e grado di vuoto.

La sezione test è un tubo orizzontale ID 80 mm nominale con un venturimetro (VFM), una sonda ad impedenza disegnata da Siet (SIET ECP) con dieci elettrodi lineari lunghi e una nuova sonda ad impedenza con elettrodi concavi (DENERG ECP). Per la presente campagna sperimentale, il range di portata d'aria è $0,048 - 0,019 kg/s$ (velocità superficiale 8-19 m/s) e $0 - 0.0535 kg/s$ (0-192 l/h) per l'acqua (intervallo di velocità superficiale da $0,0006 m/s$ a $0,0103 m/s$). Questi intervalli di velocità superficiali corrispondono a regimi di deflusso (flow patterns) stratificato-ondulato e anulare-disperso lungo la sezione di test.

Questo lavoro di tesi è diviso in tre sezioni principali. La prima presenta la descrizione del deflusso bifase (modelli, classificazioni dei regimi di deflusso, definizione dei principali parametri e variabili utilizzati, ecc ...), le ragioni per cui è necessario sviluppare il cosiddetto Spool Piece (SP) costituito da diversi dispositivi per misurare i parametri bifase e una panoramica generale sui misuratori di pressione differenziale e sulle sonde ad impedenza. Nella seconda vengono descritti in dettaglio l'apparato sperimentale, la sezione test, la strumentazione con la relativa calibrazione e il metodo di acquisizione dei segnali. Nella terza sezione viene presentata la campagna sperimentale con la matrice sperimentale e le procedure di test per caratterizzare i segnali di VFM, SIET ECP e DENERG ECP. Infine, nell'ultima sottosezione della terza sezione vengono stimati la portata totale e la portata delle singole fasi in base ai risultati della presente campagna sperimentale.

Infatti, l'obiettivo finale è quello di combinare i segnali degli strumenti per ottenere la portata senza la necessità dell'osservazione visiva come nel caso di un tubo opaco.

Chapter 1

Introduction

Two-phase flow is becoming increasingly important in many processes and power-generation technologies, particularly in nuclear energy, oil and gas and chemical processing industries.

It's, however, by no means limited to today's modern industrial technology, and multiphase flow phenomena can be observed in a number of biological systems and natural phenomena which requires better understanding [1].

Common single-phase classification is not sufficient to describe the nature of two-phase flows. The complex nature of two-phase flow, especially gas-liquid flow, originates from the existence of multiple, deformable and moving interfaces and attendant discontinuities of fluid properties and complicated flow field near the interface [2].

In fact, the two-phase flow physics are multi-scale in nature. At least there are four different scales [1]:

- **system scale** where system transients and component interactions are the primary focus;
- **macroscopic scale** related to structures of interface and the transport of mass, momentum and energy;
- **meso scale** related to local structures;
- **microscopic scale** related to fine structures and molecular transport.

Despite the abundance of single-phase measurement devices relying on different physical principles, a universal device for two-phase flow rate measurement is still lacking. This is due to the fact that the flow is governed by several parameters (flow pattern identification, void fraction, phases velocities, etc.) which cannot be measured by a single instrument.

For this reason, the development of a Spool Piece (SP) is under study. In general, a SP consists of a series of different instruments that are used to acquire different signals needed to measure and recognize two-phase phenomena.

To accurate model of two-phase systems reliable measurements of the void fraction and flow pattern identification is important. Different techniques, depending on the applications, can be used to measure void fraction. For example, radiation attenuation (X or γ -ray or neutron beams) for line or area averaged values, optical or electrical contact probes for local void fraction, impedance or capacitance sensors for time and volume averaged void fraction and quick-closing valves for direct volume measurement. The radiation attenuation method can be expensive and difficult to implement from the point of view of safety, while the impedance measurement technique is non-intrusive and relatively simple to design and implement [2].

Electrical impedance or capacitance probes have been used successfully to measure time and volume averaged void fraction, and its instantaneous output signal to identify flow pattern [3]. This devices can be coupled with traditional flow rate measurement instruments such as a Venturi flow meter (VFM) to form a SP.

Different devices have been coupled with the VFM to form a SP in the studies previously carried out at Dipartimento Energia (DENERG) of Politecnico di Torino [4]. An electrical capacitance probe with nine external long linear electrodes and one internal central electrode, designed by SIET (SIET ECP) was originally used, which allowed to get information on the phases distributions inside the probe volume, but required a very complex elaboration of 10 different signals. Moreover, the SIET ECP did not provide the average void fraction in the test section but the average linear void fraction along 9 different radii and all the possible cords between the different circumferential electrodes. In order to obtain directly this average void fraction, two new Electric Capacitance Probes with concave electrodes have been developed at DENERG (DENERG ECP) and added to the SP.

This thesis work is divided into four main sections.

The first one presents the description of the two-phase flow (models, classifications of flow patterns, definition of the main parameters and variables used, etc...), reasons why it is necessary to develop the so called Spool Piece (SP) constituted by several devices to measure two-phase parameters and a general overview on the differential pressure meters and impedance probes. In the second one the experimental facility, the test section, the instrumentation with their calibration and the method of acquisition of signals are described in detail.

In the third section the experimental campaign with the experimental matrix and the test procedures to characterized the signals of VFM, SIET ECP and

DENERG ECP.

Finally, on the last subsection of the third section, are estimate the total flow and the individual flow of the single phases, based on the results of the present experimental campaign.

In fact, the final goal is to combine the signals of the instruments to get the flow rate without the needing of the visual observation, such as in the case of an opaque pipe.

Chapter 2

Two-phase flow

The expression of “two-phase flow” is used to describe the simultaneous flow of two different liquid, a gas and a liquid, a gas and a solid or a liquid and a solid. Gas-liquid flow, among these types, has the most complexity due to the deformability and the compressibility of the phases [2]. Common single-phase flow regime classification are not sufficient to describe the nature of two-phase flows. The two-phase flow physics are multi-scale in nature. At least there are four different scales [1]:

- **system scale** where system transients and component interactions are the primary focus;
- **macroscopic scale** related to structures of interface and the transport of mass, momentum and energy;
- **meso scale** related to local structures;
- **microscopic scale** related to fine structures and molecular transport.

Moreover, there are an infinite number of ways in which the interfaces can be distributed within the two-phase flow so is difficult to understand, predict and model.

2.1 Models

In internal gas and liquid mixture flow, gas and liquid are in simultaneous motion inside the pipe so the resulting two-phase flow is physically more complicated than single-phase flow. In addition to the usual inertia, viscous and and pressure forces (present in single-phase flow) it is necessary to consider the interfacial tension forces, the wetting characteristics of the liquid on the

tube wall and the exchange of momentum between the liquid and gas phases in the flow. So the gas-liquid flow is a complex three-dimensional transient problem since the flow conditions in a pipe vary across its length, over its cross section and with time[5].

Three main methods are used to analyze a two phase flow [6]:

- **The homogeneous flow model.** The two-phase flow is assumed to be a single-phase flow having pseudo-properties obtained by suitably weighting the properties of the individual phases, considering the phases flowing with the same velocity.
- **The separated flow model.** The two phases of the flow are considered to be separated by the interfaces. Two sets of basic equations are written, one for each phase or, alternatively, the equations can be combined.
- **The flow pattern model.** It is a more sophisticated approach where the two phases are considered to be arranged in one of three or four definite prescribed phases distribution geometries, which are based on the various flow patterns found when a gas and a liquid flow together in a channel. In order to apply these models it is necessary to be able to predict the transition from one pattern to another.

2.2 Horizontal flow pattern classification

In determining the horizontal flow pattern important physical parameters are [5]:

- *Surface Tension*- which keeps pipe walls always wet and tends to make small liquid drops and small gas bubbles spherical.
- *Gravity*- the phases tend to separate due to difference in density and the heavier (liquid) phase tend to accumulate at the bottom of the pipe.

The major flow regime in gas-liquid flow in horizontal pipes are summarized in Fig.2.1. From top to bottom [7]:

- **Stratified flow.** At low liquid and gas velocities, complete separation of the two phases occurs. The gas goes to the top and the liquid to the bottom of the pipe, separated by an undisturbed horizontal interface.

- **Wavy flow.** Increasing the gas velocity in a stratified flow, waves are formed on the interface and travel in the direction of flow. The amplitude of the waves is notable and depends on the relative velocity of the two phases; however, their crests do not reach the top of the pipe. The waves climb up the sides of the pipe, leaving thin films of liquid on the wall after the passage of the wave.
- **Intermittent flow.** Further increasing the gas velocity, these interfacial waves become large enough to wash the top of the pipe. This regime is characterized by large amplitude waves intermittently washing the top of the tube with smaller amplitude waves in between. Large amplitude waves often contain entrained bubbles. The top wall is nearly continuously wetted by the large amplitude waves and the thin liquid films left behind. Intermittent flow is also a composite of the plug and slug flow regimes:
 - **Plug flow.** This flow regime has liquid plugs that are separated by elongated gas bubbles. The diameters of the elongated bubbles are smaller than the pipe such that the liquid phase is continuous along the bottom of the pipe below the elongated bubbles.
 - **Slug flow.** At higher velocities, the diameters of elongated bubbles become similar in size to the channel height. The liquid slugs separating such elongated bubbles can also be described as large amplitude waves.
- **Annular flow.** At even larger gas flow rates, the liquid forms a continuous annular film around the perimeter of the tube, the liquid film is thicker at the bottom than the top. The interface between the liquid annulus and the vapor core is disturbed by small amplitude waves and droplets that may be dispersed in the gas core. At high gas fractions, the top of the tube with its thinner film becomes dry first, so that the annular film covers only part of the tube perimeter and thus this is classified as stratified-wavy flow.
- **Dispersed bubble flow.** The vapour bubbles tend to travel in the upper half of the pipe; at moderate velocities both vapour and liquid phases cover the pipe cross-section.

The main task is to predict which flow pattern will exist under any set of operating conditions and the value of the characteristic fluid and flow parameters at which the transition from one flow pattern to another will take place.

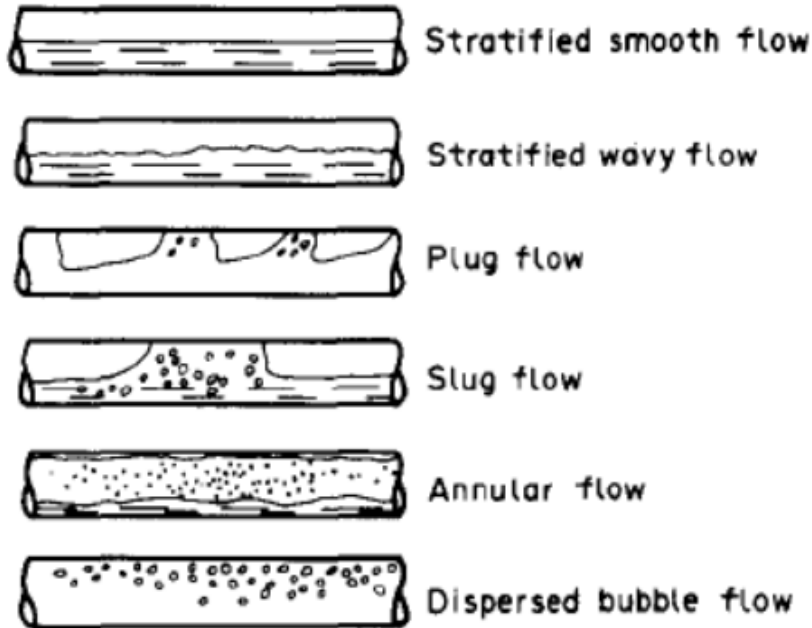


Figure 2.1: Schematic representation of horizontal flow regimes [6].

2.3 Definitions of variables used in two-phase flow

The parameters that govern the occurrence of a given flow pattern are numerous, the most important are flow rates, fluid properties of each pipe, pipe geometry and inclination. The total mass flow rate W_{tot} , the volumetric flow rate Q_{tot} , and the mass flux or mass velocity G_{tot} , are defined as:

$$W_{tot} = W_l + W_g \quad (2.1)$$

$$Q_{tot} = Q_l + Q_g = \frac{W_l}{\rho_l} + \frac{W_g}{\rho_g} \quad (2.2)$$

$$G_{tot} = G_l + G_g = \frac{W_l}{A} + \frac{W_g}{A} \quad (2.3)$$

and the volumetric flux or superficial velocity:

$$J_{tot} = J_l + J_g = \frac{G_l}{\rho_l} + \frac{G_g}{\rho_g} \quad (2.4)$$

The flow quality x and the volumetric quality β is defined as:

$$x = \frac{W_g}{W_l + W_g} \quad (2.5)$$

$$\beta = \frac{Q_g}{Q_l + Q_g} \quad (2.6)$$

One of the most important parameters used to characterize two-phase flow is the void fraction α , a dimensionless quantity indicating the fraction of a geometric or temporal domain occupied by the gaseous phase. It is necessary to calculate other important parameters such as the hydrostatic and accelerational pressure drop of the flow. Different geometric configuration are used to specify the void fraction: local, chordal, cross-sectional and volumetric. Furthermore, those quantities can be defined as instantaneous or time averaged values. The local time averaged void fraction refers to a point or very small volume:

$$\alpha_{local}(r) = \frac{1}{t} \int P(r, t) dt \quad (2.7)$$

where $P(r,t)$ represent the local instantaneous presence/absence of gas at some point r at the time t and $P(r,t)=1$ for gas phase , $P(r,t) =0$ for liquid phase. The chordal void fraction is defined as:

$$\alpha_{chordal}(t) = \frac{L_g}{L_g + L_l} \quad (2.8)$$

where L_g is the length of the line through the gas phase and L_l is the length of the line through the liquid phase. The cross-sectional void fraction is defined as:

$$\alpha_{cross-sectional}(t) = \frac{A_g}{A_g + A_l} \quad (2.9)$$

where A_g is the area occupied by the gas phase and A_l is the area occupied by the liquid phase. The volumetric void fraction is:

$$\alpha_{volume}(t) = \frac{V_g}{V_g + V_l} \quad (2.10)$$

where V_g is the volume occupied by the gas phase and V_l is the volume occupied by the liquid phase. The relation between flow quality and void fraction is:

$$x = \frac{W_g}{W_g + W_l} = \frac{U_g A_g \rho_g}{U_g A_g \rho_g + U_l A_l \rho_l} = \frac{\alpha U_g \rho_g}{(1 - \alpha) U_l \rho_l + \alpha U_g \rho_g} = \frac{\alpha}{\frac{(1-\alpha)}{\alpha} \frac{\rho_l}{\rho_g} \frac{1}{S} + 1} \quad (2.11)$$

where U_l and U_g are the real velocities of the two phases. S is called slip ratio and represents the ratio between the real velocity of the gaseous phase and the real velocity of the liquid phase and can be local and instantaneous or averaged in space and/or time [8].

2.4 Flow pattern maps and transitions

Usually flow patterns are recognized by visual inspection, though other methods have been devised for those circumstances in which visual information is difficult to obtain.

For some of the simpler flows (vertical or horizontal pipes) a substantial number of investigations have been conducted to determine the dependence of the flow pattern on superficial phase velocities or generalized parameters containing these velocities. The results are displayed in the form of a flow regime map. The boundaries between the various flow patterns in a flow pattern map occur because a regime becomes unstable as the boundary is approached and growth of this instability causes transition to another flow pattern. Multiphase transitions can be rather unpredictable since they may depend on many features of the flow. So, the flow pattern boundaries are not distinctive lines but just transition zones.

One of the serious difficulties, with almost all the existing literature, is that these maps are often dimensional and therefore apply only to a specific pipe sizes and fluids. Despite the issues discussed, it is useful to provide a regime map that help to distinguish the various regimes [6].

2.4.1 Taitel and Dukler's map

The Taitel and Dukler's map (Taitel and Dukler, 1976), shown in Fig.2.2, is the most widely used flow pattern map for horizontal two-phase flow; it is based on a semi-theoretical method and it is computationally more difficult to use than others [9]. The horizontal coordinate of the map is the Lockhart–Martinelli parameter (Lockhart and Martinelli, 1949), the vertical coordinates are K on the left hand side and T or F on the right hand side that are defined as follows:

$$X = \left[\frac{\frac{4 \cdot C_L}{D} \cdot \left(\frac{j_L \cdot D}{\nu_L} \right)^{-n} \cdot \frac{\rho_L \cdot (j_L)^2}{2}}{\frac{4 \cdot C_G}{D} \cdot \left(\frac{j_G \cdot D}{\nu_G} \right)^{-m} \cdot \frac{\rho_G \cdot (j_G)^2}{2}} \right]^{0.5} \quad [-] \quad (2.12)$$

$$F = \sqrt{\frac{\rho_G}{\rho_L - \rho_G}} \cdot \frac{j_G}{\sqrt{D \cdot g}} \quad [-] \quad (2.13)$$

$$K = F \cdot \left[\frac{D \cdot j_L}{\nu_L} \right]^{0.5} = F \cdot [Re_L]^{0.5} \quad [-] \quad (2.14)$$

The Lockhart–Martinelli parameter depends on the parameters C_L , C_G , n and m . The authors take the values of this parameters which correspond to

turbulent gas and turbulent liquid flow, which is the case of greatest practical interest ($n = m = 0.2$, $C_G = C_L = 0.046$) and use different coordinates for each transition boundary:

- stratified to annular: X,F
- stratified to intermittent: X,F
- intermittent to dispersed bubble: X,T
- stratified smooth to stratified wavy: X,K

With this method of mapping, the boundaries are relatively insensitive to the pipe diameter for an air-water system at low pressure and small line sizes.

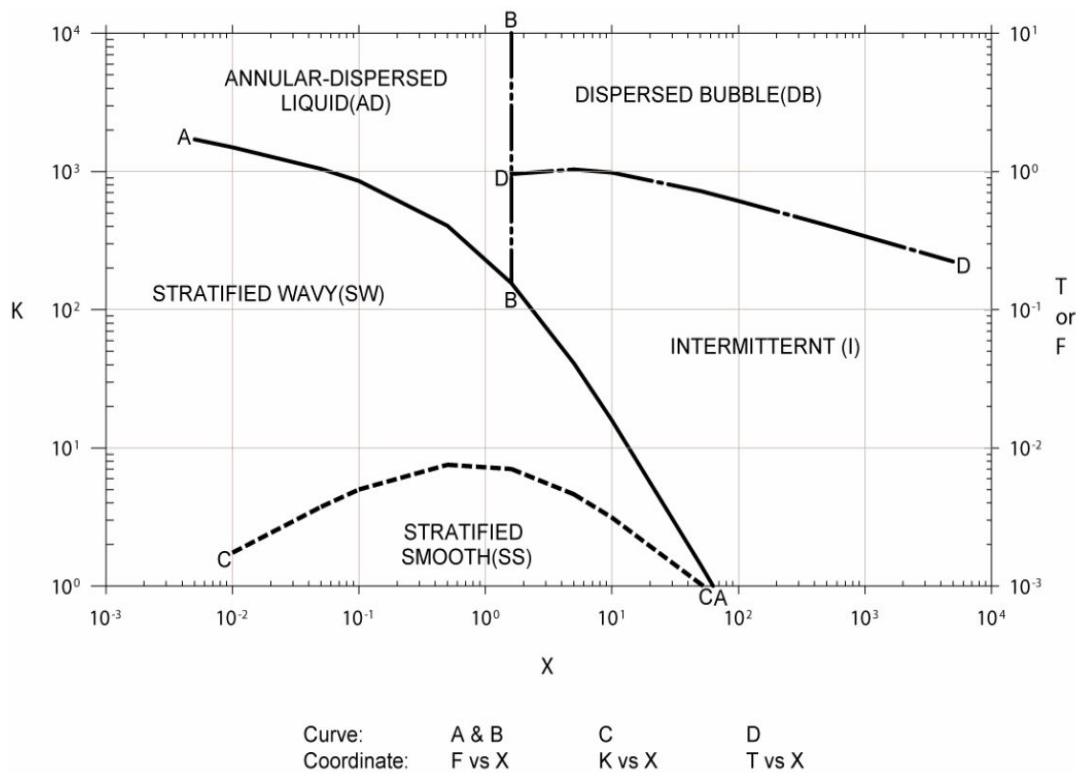


Figure 2.2: Taitel and Duckler's map for horizontal tubes [9].

2.5 Void fraction correlations

Void fraction correlations have been developed in the literature for over 60 years. Due to the large number of correlations available in literature, many research studies have focused on the comparison of performances of different void fraction correlations when tested against some experimental data.

A review of such data by [10] shows that the more accurate for horizontal flow is Chisholm's correlation.

Chisholm's Correlation[10]

Chisholm (1969) developed a two-phase flow correlation, considering the slip between the fluids. It was assumed an incompressible two-phase flow, with negligible upstream momentum, no phase change, irrelevant drag forces in the wall when compared to the interfacial forces between the phases, and a constant void fraction across the differential pressure device. The total mass flow rate W_{tot} with Chisholm's correlation is defined by:

$$W_{tot-Chisholm} = W_g(1 + C\chi_{mod} + \chi_{mod}^2) \quad (2.15)$$

where W_g is the gas flow rate, C , χ_{mod} (modified Lockart-Martinelli parameter)

$$C = \frac{1}{S} \left(\frac{\rho_l}{\rho_g} \right)^{0.5} + S \left(\frac{\rho_g}{\rho_l} \right)^{0.5} \quad (2.16)$$

$$\chi_{mod}^2 = \left(\frac{1-x}{x} \right) \left(\frac{\rho_l}{\rho_g} \right)^{0.5} \quad (2.17)$$

and S is the slip ratio is assumed equal to:

$$S = \left(\frac{\rho_l}{\rho_g} \right)^{\frac{1}{4}} \quad (2.18)$$

Chisholm concluded that the meter response to two-phase flow in horizontal pipe not only depend on the modified Lockart-Martinelli parameter, but also on the gas-liquid density ratio (and then on the pressure).

2.6 Spool Piece (SP)

So, in two-phase flow in pipes there are two parameters of significance [5]:

- pressure drops;
- void fraction.

Measurement of pressure drops Among the most important techniques available for measuring pressure drop are:

- *Pressure drop measurement using subtraction of signals from two locally mounted pressure transducers* - The problem with this method is that signals from two separate instruments are being measured and subtracted, and this increases error.
- *Pressure drop measurement using differential pressure transducers* - These types of transducers have a sensitivity of about 0.1% to 0.3% full scale, a response time of about 10 to 200 μs and are very stable.

Measurement of void fraction Void fraction measurement is important in the calculation of pressure gradients and in the calculation of the amount of liquid and gas present in a system. There are four main types of void fraction measurement:

- *Pipe-average measurements*- A practical method is the use of quick-closing valves placed at the beginning and end of a section of pipe over which the void fraction is to be determined and simultaneously operated. Actuating the valves the liquid phase trapped in the pipe is drained and its volume measured. Since the pipe volume can be estimated, the pipe-averaged void fraction can be found.
- *Cross-sectional average measurement*- The average void fraction is sought over a given pipe cross section by using traversable single-beam radiation absorption methods, multibeam radiation absorption techniques, or neutron-scattering techniques.
- *Chordal-average void fraction measurements*- The average void fraction is measured across the diameter of a pipe by using radiation absorption methods.

- *Local void fraction measurements*- Void fraction is measured at a particular position within the pipe using local optical or electrical void probes.

As already mentioned, there is not a single instrument which will measure these fundamental parameters directly but it is necessary to couple several devices in a so called Spool Piece (SP). There are a lot of possibilities of combining different instruments to set up the SP; in the last decades, a lot of efforts were directed to develop a SP with only two instruments, with the advantage of reducing the total lengths and of course the costs and the complexity of the installation. The drawback of reducing the number of instruments is the need to compensate for the missing information through empirical or theoretical models and correlations.

In general, a SP generate a set of signals proportional to physical quantities (mechanical, thermal, electrical, etc.) whose analysis leads to the estimation of the flow rates with adequate accuracy and reliability.

A quick reference for the estimation of the characteristic parameters of the two-phase flow presupposes [11]:

- the definition of the instruments installed in the SP from a geometric and constructive point of view;
- the lengths and diameters of the calm sections upstream and downstream of each instrument;
- the lengths and diameters of the pipes upstream and downstream of the SP;
- the electronics with the conversion law signal-physical quantity associated with each instrument of the SP;
- the arrangement of the SP (horizontal, vertical, inclined);
- the availability of experimental campaigns, with single-phase and two-phase flow, to characterize the SP;
- the availability of an adequate software able to interpret the acquired signals.

So, the choice of a meter composing the SP depends on the purpose for which the measurement is made, whether is needed an average or a local quantity and on the accuracy required. To evaluate the accuracy of the measure the entire acquisition system must be considered: the measured parameters

transferred through the sensor, are converted from analogical to digital electric signal and sent to the PC through the Data Acquisition (DAQ). Voltage spikes, spurious noise, pressure and temperature spikes should be addressed as to their possible negative effects and mitigated [12].

So, to recap, the design of the SP is very important and the fundamental criteria for the first selection were [8]:

- range of measurement,
- dynamic response,
- installation requirements,
- materials compatibility with pressure and temperature conditions.

The analyzed devices are:

- Venturi Flow Meter,
- Impedance Probes .

2.6.1 Differential pressure meters

In industrial application the calculation of fluid flow rate by reading the pressure loss across a pipe restriction is the most commonly used flow measurement technique. In the last decades, many investigations focused on air-water two-phase flow measurement use the orifice plate and Venturi Flow Meter (VFM). The VFM has a lot of advantages: little influence on flow regimes, smallest pressure loss and shortest straight pipe upstream and downstream[13].

The classical Herschel Venturi (Fig. 2.3) has a very long flow element characterized by a tapered inlet and a diverging outlet. The entrance is a converging cone with a 15° to 20° angle; it converges down to the throat, which is the point of minimum cross-sectional area, maximum velocity, and minimum pressure in the meter. The exit portion of the meter is a diverging cone with an angle of 5° to 7° which completes the transition back to full pipe diameter [8].

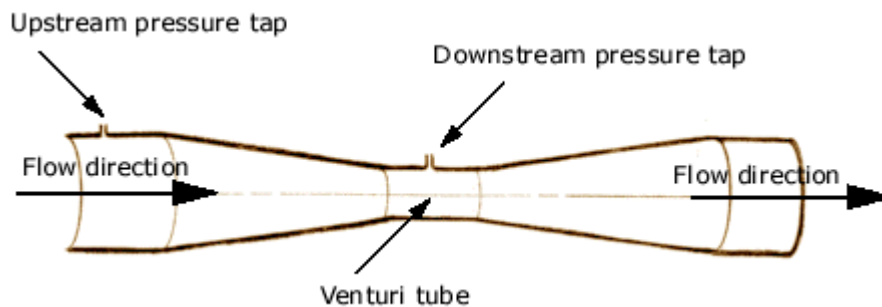


Figure 2.3: Classical Venturi Flow Meter [14]

In the short form Venturi (Fig. 2.4-A), the entrance angle is increased; it maintains many of the advantages of the classical Venturi, but at a reduced initial cost, shorter length and reduced weight.

The changes in cross section area cause changes in velocity and pressure of the flow. Because of the smooth gradual transition down to the throat diameter and back to the full pipe diameter, the friction loss in a VFM is quite small. VFMs are insensitive to velocity profile effects and therefore require less straight pipe run than an orifice. Venturi tubes are available in sizes up to 72", the flow rate through it is 25-50% greater than the flow rate through an orifice with the same pressure drop.

Furthermore, the total unrecovered head loss rarely exceeds 10% of measured pressure drop (Figure 2.5) [14].

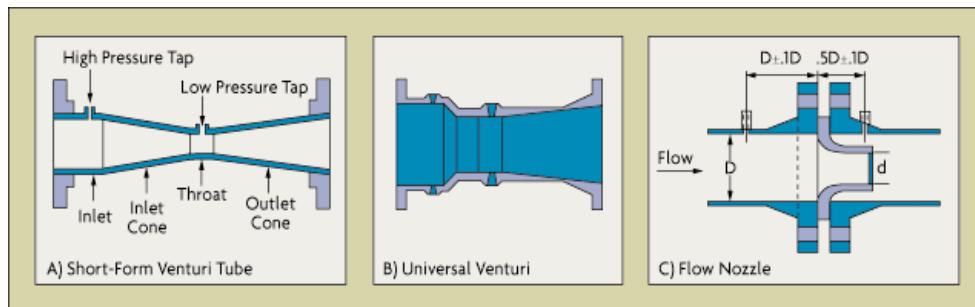


Figure 2.4: Venturi flow meter types [14].

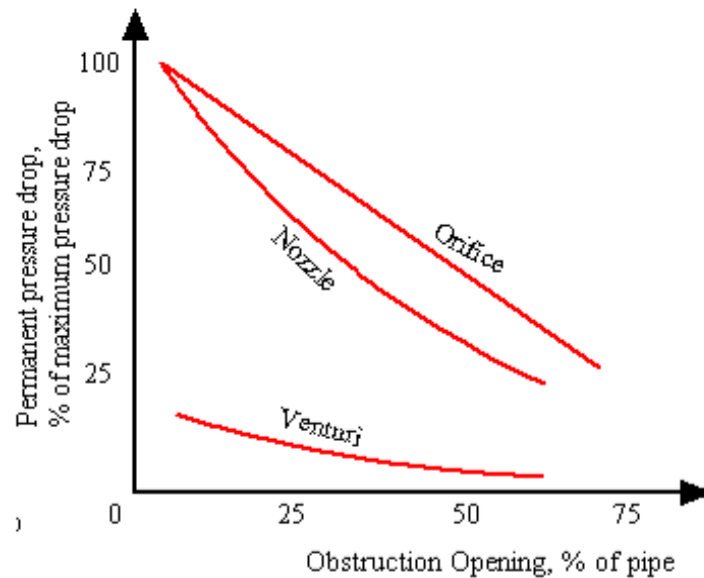


Figure 2.5: Permanent pressure drop in differential flow meter [14].

Their smoothed geometry makes the device immune to corrosion and erosion so that it is characterized by very low installation and operating and

maintenance costs.

Starting from the Bernoulli's equation that established the relationship between static and kinetic energy in a flowing stream, the general Differential Flow Meter equation in a two-phase flow can be written as:

$$W_{tot} = K \cdot \sqrt{2 \cdot \Delta p_{TP} \cdot \rho_{TP}} \quad (2.19)$$

where Δp_{TP} is the difference of pressure between the undisturbed upstream pressure in the pipe and the pressure in the pipe at the constricted area, ρ_{TP} is the density and the coefficient K:

$$K = \frac{C_d \cdot F_a \cdot Y}{\sqrt{1 - \beta^4}} \cdot A_2 \quad (2.20)$$

where C_d is discharge coefficient for the particular meter, F_a is thermal expansion correction factor, Y is the compressibility coefficient, β is the diameter ratio between the throat diameter of the flow meter and the inside diameter of the pipe and A_2 the constricted area.

The numerical values of F_a for orifice plates given in ISO5167 are based on data determined experimentally. Instead for Venturi tubes they are based on thermodynamic general energy equation depending on the device geometry. The discharge coefficient C_d , influenced by the Reynolds number, β and additional parameters depending on the type of flow element used, is determined by laboratory tests or in-place calibration if better accuracy is required.

The use of an differential meter with two-phase flow causes an increase in the measured differential pressure because of the interaction between the gas and the liquid phase, so that the single-phase formulation overpredicts the effective flow rate. It's necessary to correct the over-reading using available correlations derived from experimentally data to determine the actual gas mass flow rate. There are three approaches [15]:

- adjusting the value of density to reflect the presence of a second component;
- adjusting the discharge coefficient to introduce the presence of the second component;
- relating two-phase pressure drop to that which would have occurred if all the flow were passing either as a gas or as liquid.

So, the two parameters that have to be defined are the two-phase discharge coefficient and the two-phase density. The correction of the density can be made considering either the homogeneous flow correlation or the separated

flow correlation or James' correlation (a modification of the homogeneous correlation).

The most used approach, in case of two-phase flow with $\alpha > 95\%$, is the third one based on the work of Lockhart and Martinelli that investigated the relation between the pressure drop in single-phase flow (subscript k) and in two-phase flow through the so called two phase multiplier:

$$\frac{\left(-\frac{dp}{dz}\right)_{TP}}{\left(-\frac{dp}{dz}\right)_k} = \phi_k^2 \quad (2.21)$$

The Lockart-Martinelli parameter is defined as:

$$\chi^2 = \frac{\left(-\frac{dp}{dz}\right)_l}{\left(-\frac{dp}{dz}\right)_g} \quad (2.22)$$

Assuming that the two phases are flowing under turbulent regime and using the Blasius correlation for the single-phase friction factor coefficients calculation the parameter χ^2 can be written as:

$$\chi^2 = \left(\frac{(1-x)}{x}\right)^{0.875} \cdot \left(\frac{\rho_g}{\rho_l}\right)^{0.5} \cdot \left(\frac{\mu_l}{\mu_g}\right)^{0.125} \quad (2.23)$$

For a two-phase mixture flowing in orifice and Venturi devices the parameter is usually written as:

$$\chi^2 = \left(\frac{\rho_g}{\rho_l}\right)^{0.5} \cdot \left(\frac{\mu_l}{\mu_g}\right)^{0.125} \quad (2.24)$$

Using this approach the total mass flow rate in the VFM can be written as:

$$W_{tot} = K_{TP} \cdot \sqrt{2 \cdot \Delta p_{TP} \cdot \rho_{TP}} = K_k \cdot \sqrt{2 \cdot \Delta p_k \cdot \phi_k^2 \cdot \rho_k} = W_k \cdot \phi_k \quad (2.25)$$

The correlations currently available for the two-phase flow signal correction have been derived from a limited set of data and may only be suitable to cover restricted ranges of the flow meter parameters, for example, a specific diameter ratio and are closely dependent on experimental conditions such as pressure, temperature etc. The use of correlations outside the conditions used to define them can result in large errors in the calculation of the gas mass flow rate.

2.6.2 Impedance probes

The impedance technique (conductance or capacitance) has often been applied in two-phase flow research to measure void fraction [3]. Because of the fast response of the impedance meter it is possible to obtain information about virtually instantaneous void fractions and their distributions across a pipe section.

The impedance method is based on the fact that the liquid and gas phases have different electrical conductivity and relative permittivity, and the electrical impedance of a mixture is usually different by the impedance of each component. The gases are generally poor conductors with a low dielectric constant, while the liquids, although not good conductors, assume higher value of the dielectric constant due to a greater concentration of dipoles.

From an economic point of view this technique respect to others is more convenient; in addition, the void meter can be constructed in a non-intrusive structure. Instead one of the most important drawbacks is the strong sensitivity to the flow pattern.

The measurements of the void fraction with impedance sensors are quasi-local: the sensor determines the percentage of both phases not strictly in a selected cross section of the pipe but in a certain volume, not precisely drawn due to the fringe effects, defined by the lines of an electric field associated with the electrode system.

Fringe effects

A voltage difference applied between two conductive objects results in an electric field between them. This electric field exists not just between plates, but extends some distance away. This is called Fringe effects. So, the exact boundary of the volume, based on the electrodes height, cannot be precisely drawn. To minimize the non-local effects, the height of the electrodes measured along the pipe should be as short as possible, but the effect of the fringe field cannot be eliminated. Short electrodes have, however, small capacitance and low sensitivity, and in this case a compromise is needed.

Concerning the electrodes geometry, many different configuration were studied by a number of authors. Selecting the optimum shape is not a simple task. In fact, the relationship between void fraction and impedance depends on flow regime.

Ahmed [16] presented a systematic method for the design of capacitance sensors for void fraction measurement and flow pattern identification. Two different configurations of the sensors were considered: concave and ring type (Fig.2.6). For the ring types sensor each electrode covers the entire circum-

ference, except for a small gap to facilitate the installation of the sensor around the tubes, and are separated in the axial direction of the tube, while in the concave sensor, two brass strips are mounted on the tube circumference opposite to each other.

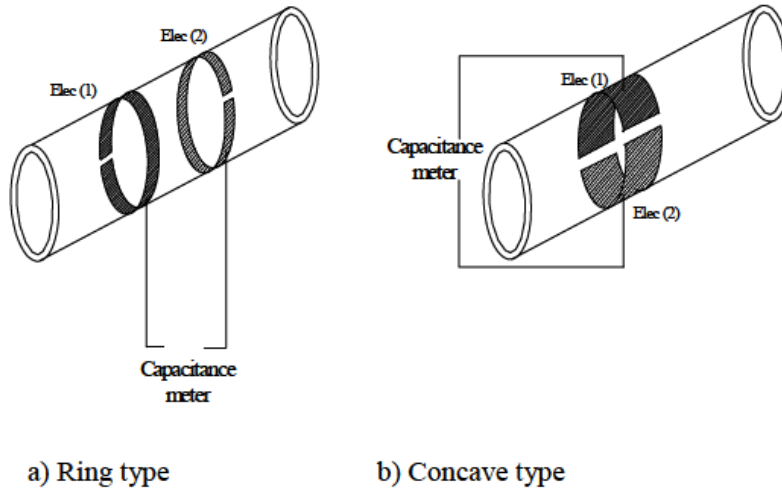


Figure 2.6: Scheme of ring and concave type sensor [16].

Ahmed [16] showed that the relationship between the capacitance and the void fraction is dependent on the dielectric values of the two phases, but also on the cross-sectional area of the sensors, and the separation distance between the two electrodes.

Therefore, the impedance technique is non-intrusive and simple to design and implement. However, there are several disadvantages:

- sensitivity to the void fraction distribution or flow regime due to the non-uniformity of the electric field inside the measuring volume;
- sensitivity to the changes in electrical properties of the two phases due to temperature;
- the noise due to electromagnetic field around the sensor and connecting wires.

The first problem can be solved by first identify the flow pattern while the last can be minimized through proper design of the sensor shield.

Chapter 3

Experimental facility, instrumentation

This chapter presents the configuration of the experimental facility and describes in detail the instrumentation and their calibration.

Considering the experimental facility, Fig.3.1 and 3.2, it is composed by an air supply circuit, a demineralized water supply circuit, a test section with the Spool Piece (SP) and two pneumatic quick-closing valves for the volume-averaged void fraction measurement, a water/air separator and the instrumentation for the measurement of single-phase fluids flow rate, pressure and temperature. The air is fed to the test section by a blower (UNIJET500), whose rotation frequency is fixed by an inverter, while the water is supplied by a tank thanks to gravity. The mixing zone of the two fluids is located a few centimeters upstream the inlet guillotine valve. The air enters axially, whereas the water is injected radially. The water mass flow rate is measured by a rotameter, while the air flow rate is measured by a calibrated orifice flow meter. The apparatus is transparent to allow the visual observation of the flow conditions.

For the present experimental campaign, the flow rates are from $0.048 - 0.0119\text{kg/s}$ for air (superficial velocity's range 8-19 m/s) and $0 - 0.0535\text{kg/s}$ (0-192 l/h) for water (superficial velocity's range $0.0006 - 0.0103\text{m/s}$) as shown in Table 3.1.

$f_{inverter}$ [Hz]	Wg [kg/s]	WI [kg/s]
20-30-35-40-50	0.048 – 0.070 – 0.079	0.0040 – 0.0085 – 0.0140
	0.088 – 0.119	0.0210 – 0.0290 – 0.0390 – 0.0540

Table 3.1: Experimental matrix.

The experimental void fraction's range is $0.976 - 0.997$ and flow quality's

range is 0.60 – 0.96. The resulting flow patterns are wavy stratified and dispersed annular. For the same couple of flow rates of the liquid and gas phases different separate tests have been carried out to assess the repeatability of the measurements.

Table 3.2 shows superficial velocities, flow quality, temperature of the test section inlet, temperature and the average volumetric void fraction in some typical test run.

j_g [m/s]	j_l [m/s]	x [-]	$T_{in,ECP}$ [C]	p [barg]	α [-]
12.0	0.0016	0.901	19.6	0.091	0.992
	0.0037	0.796	20.6	0.091	0.986
	0.0054	0.724	20.9	0.091	0.983
	0.0087	0.621	20.9	0.092	0.977
	0.0106	0.572	21.0	0.092	0.973
13.5	0.0018	0.902	21.5	0.127	0.992
	0.0038	0.813	22.5	0.127	0.987
	0.0054	0.757	22.7	0.127	0.984
	0.0085	0.662	23.0	0.127	0.979
	0.0102	0.618	23.0	0.128	0.976
16.0	0.0019	0.907	24.3	0.164	0.992
	0.0038	0.828	24.7	0.165	0.988
	0.0053	0.772	24.8	0.166	0.985
	0.0086	0.677	24.8	0.167	0.980
	0.0102	0.636	25.1	0.167	0.978
19.7	0.0017	0.934	26.1	0.252	0.994
	0.0039	0.858	26.5	0.253	0.990
	0.0053	0.815	25.5	0.259	0.987
	0.0091	0.719	26.2	0.258	0.982
	0.0102	0.695	25.8	0.258	0.981

Table 3.2: Typical test run.

The instruments used are a differential pressure transducer for the absolute pressure, two differential pressure transducers for the pressure drops in VFM, a differential pressure transducer for the orifice and four thermocouple. For each of them the calibration curve was constructed to correlate the electric signal to the physic quantity. These signals are acquired using the National Instruments DAQ system (NI USB 6353, NI 9213 and NI 9205) and are managed using the LabVIEW software. The static values of the signals for air and water are measured before each set of experimental runs. Then,

for each run, the water and air mass flow rates are fixed and when the flow is stabilized in the test section, pressure and temperature values and the signal from the sensors are acquired.

At the end of each run the volumetric void fraction is measured 5-10 times, with the quick closing valves, in order to have a sufficient statistics.

As regard the SIET ECP, the signals sent and received by the DAQ are managed using the LabVIEW software.

On the other hand, the signals of DENERG ECP are generated and received by an Analog Device- Evolution board AD7746 [17] (range: $\pm 4\text{pF}$) and managed by an Evolution Board Software v2.2 [18]. The measurements in the different probes and the data elaboration are synchronized by a “master” program developed in LabVIEW environment.

3.1 Test section

The test section has a total length of approximately 2900 mm and consists of all the components located between the guillotine quick-closing valves; it comprises a PMMA (PolyMethylMethacrylate) horizontal pipe with a nominal inner diameter of 80 mm, which allows the visualization of the flow, the SP and an outlet pipe. The spool-piece consists of a SIET ECP with nine external long linear electrodes and one internal central electrode, two new ECPs with concave electrodes (DENERG ECP), and the Venturi Flow Meter (VFM). The SIET ECP, whose length is 390 mm, is located approximately 700 mm downstream the inlet pneumatic valve. The pipe connecting the SIET ECP to the VFM is 995 mm long and is equipped with the two DENERG ECPs. The VFM is 340 mm long with a throat diameter of 40 mm; it is a symmetric Venturi, so both sides have the same inclination (21°). The outlet pneumatic quick-closing valve is located 495 mm downstream the VFM. The outlet pipe has the same inner diameter of the test section and is 700 mm long. Downstream the outlet pipe a tank is installed in order to separate the phases.

The test section is equipped with two pneumatic quick closing valves used to measure the average volumetric void fraction; actuating the pneumatic quick-closing valves, the liquid phase is trapped in the test section pipe and its volume can be measured by draining the trapped water. Since the pipe volume is $14.2dm^3$, the average volumetric void fraction can be determined. In the circuit the air flow rate is measured with an orifice and its differential transducer having an accuracy of 0.15% of span, while the liquid flow rate is measured by water flow meter ASA with 0.2% of span.



Figure 3.1: Picture of the experimental facility

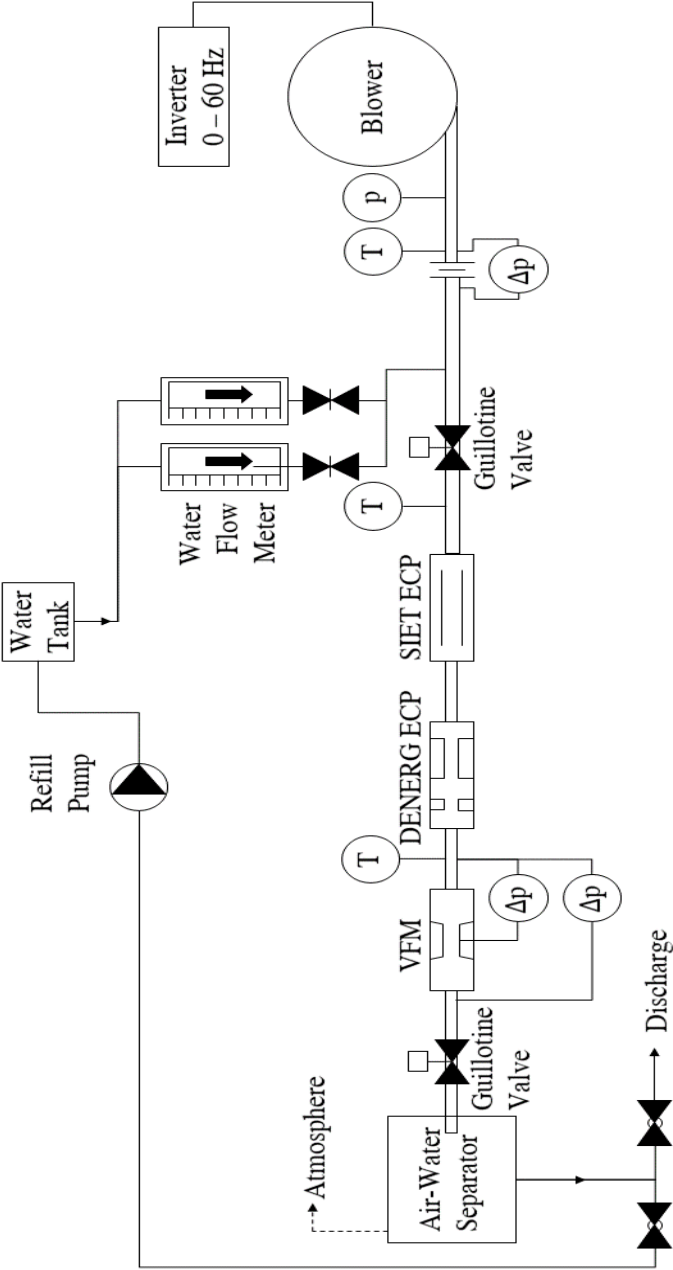


Figure 3.2: Schematic of experimental facility

3.2 Instrumentation and signals acquisition

The instruments used to measure the single phase flow parameters are:

- a differential pressure transducer for the absolute pressure;
- two differential pressure transducers for the pressure drops in VFM (Venturi flow meter):
 - between inlet-throat of VFM (reversible pressure drops, transducer accuracy 0.2% of the span);
 - between inlet-outlet of VFM (irreversible pressure drops, transducer accuracy 0.4% of the span)
- a differential pressure transducer for the orifice;
- four thermocouples (K-type, 0.5 °C accuracy):
 - at the exit of the fan (T_{in} Air);
 - at the inlet of the ECP (T_{in} ECP);
 - at the inlet of VFM (T_{in} VFM);
 - at the exit of the test section to measure the ambient temperature (T_{in} amb).

All the differential pressure transducers, used in this experimental campaign (Tab. 3.3), are characterized by a 4-20 mA current output.

Transducer	Model	Range
DP for absolute pressure (SP)	RS-PRO	0 – 750mbar
DP for orifice (SO)	Fuji Electric	0 – 3000mmH ₂ Osqrt
DP inlet-throat VFM (SV_{rev})	Rosemount	0 – 2000mmH ₂ O
DP inlet-outlet VFM (SV_{irr})	Rosemount	±620mbar

Table 3.3: Models and range of transducers.

For each of them the calibration curve was constructed to correlate the electric signal to the differential pressure by applying water columns to the transducers. Table 3.4 shows the conversion laws of the signals from volts into physical quantities:

Transducer	conversion law S in V	Units
DP for absolute pressure (SP)	$dp = 0.1882 * S - 0.1949$	<i>mbar</i>
DP for orifice (SO)	$dp = 19.243 * S^2 - 39.745 * S + 20.634$	<i>mbar</i>
DP inlet-throat VFM (SV_{rev})	$dp = 45.948 * S - 48.856$	<i>mbar</i>
DP inlet-outlet VFM (SV_{irr})	$dp = 312.57 * S - 936.51$	<i>mbar</i>

Table 3.4: Conversion laws of the signals from volt into physical quantities.

These signals are acquired using the National Instruments DAQ system (NI USB 6353, NI 9213 and NI 9205) and managed using a LabView program. The static values of the signals for air and water are measured before each set of experimental runs. Then, for each run, the water and air mass flow rates are fixed and when the flow is stabilized in the test section, pressure and temperature values and the signal from the sensors are acquired. At the end of each run the volumetric void fraction is measured 5-10 times, with the quick closing valves, in order to have a sufficient statistics.

As regard the SIET ECP, the signals sent and received by the DAQ are managed using a LabVIEW program. On the other hand, the signals of DENERG ECP are generated and received by an Analog Device- Evolution board AD7746 [17] (range: +- 4pF) and managed by an Evaluation Board Software v2.2 [18].

The measurements in the different probes and the data elaboration are synchronized by a “master” program developed in LabVIEW environment.

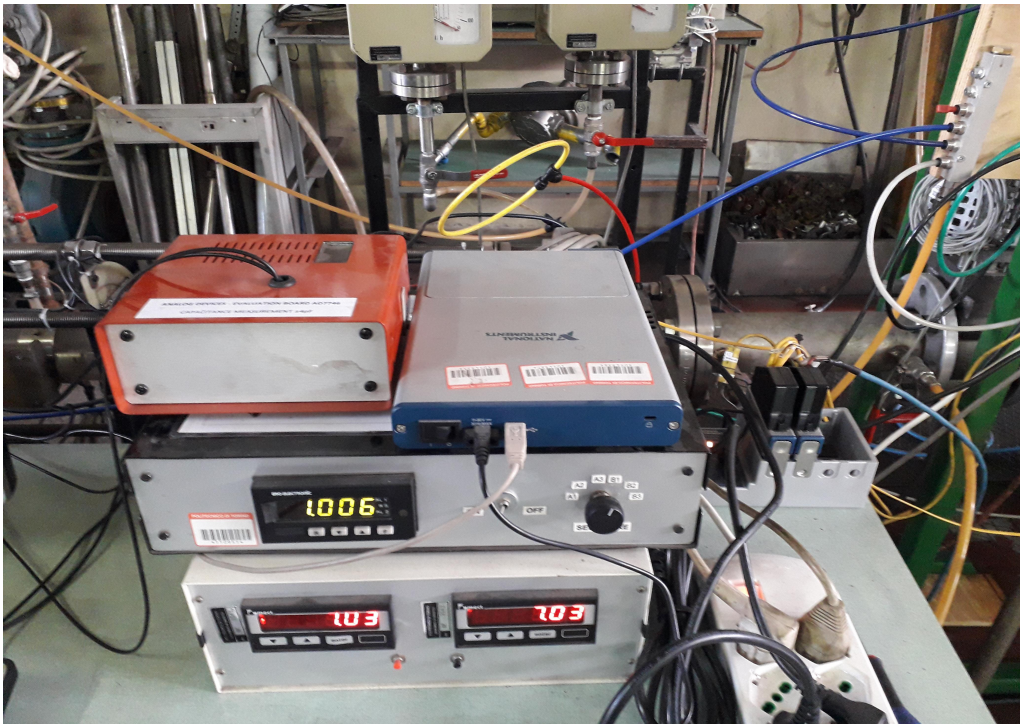


Figure 3.3: Picture of the National Instrument DAQ system and Analog Device-Evolution board AD7746.



Figure 3.4: Evolution Software v2.2 [18].

3.3 Spool Piece

There are a lot of possibilities of combining different instruments to set up the SP; in the last decades, a lot of efforts were directed to develop a SP only with two instruments, with the advantage of reducing the total lengths and of course the costs and the complexity of the installation. The drawback of reducing the number of instruments is the need to compensate for the missing information through empirical or theoretical models and correlations. Different devices have been coupled to form a SP in the studies previously carried out at Dipartimento Energia (DENERG) of Politecnico of Torino [4]. In this activity the SP consists of the venturi flow meter (VFM), the electrical capacitance probe designed by SIET (SIET ECP) and two new capacitance probe with concave electrodes' sensor (DENERG ECP).

3.3.1 Venturi Flow Meter VFM

The Figure 3.5 shows the technical design of the short form of VFM used in the present study, while the geometrical and functional characteristics are shown in Table 3.5:

Parameter	Value	Units
diameter D	80.0	mm
area A	0.00502654	m ²
minimum cross-sectional diameter d	40	mm
cross section area Ad	0.001257	m ²
$\vartheta_{convergent} = \vartheta_{divergent}$	21	°
L_{tot}	340	mm
$L_{upstream}$	628	mm
$L_{downstream}$	628	mm

Table 3.5: Parameters of the VFM.

The short form of Venturi (Fig.3.6) has been designed and built in plexi-glass according to the criteria of the UNI standards, with a divergent angle equal to the convergent. Compared to the classic venturi it has an angle of divergent above 15°; this choice reduces manufacturing costs but leads to higher irreversible pressure drops due to the detachment of the fluid line.

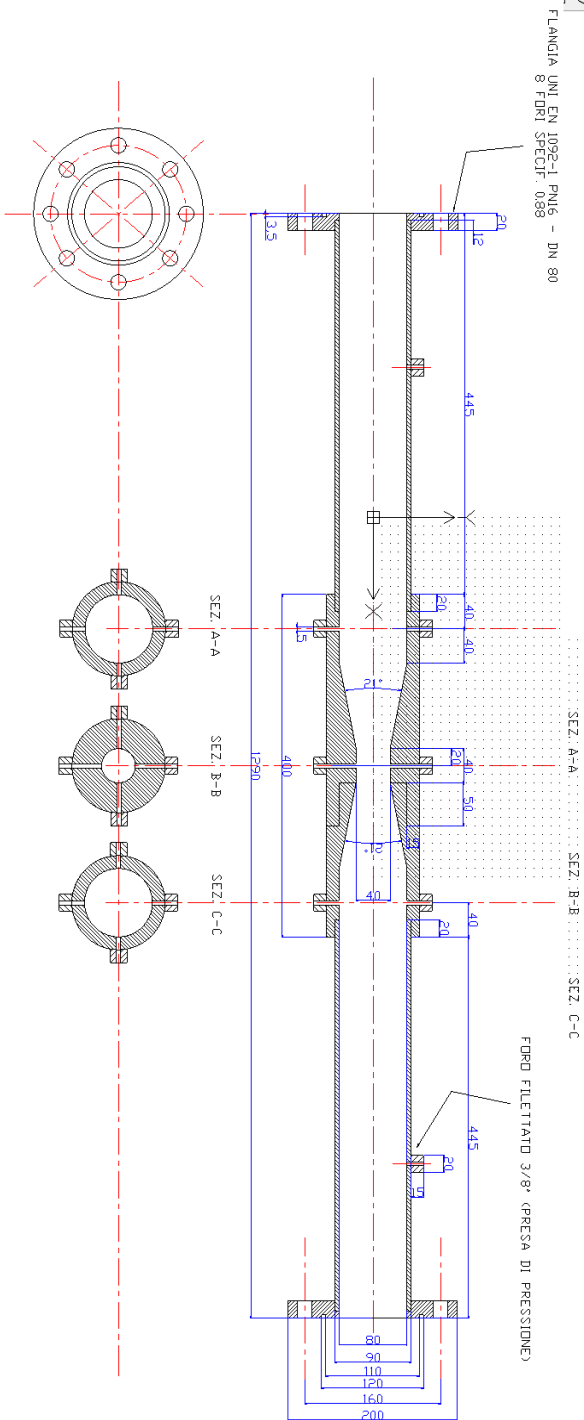


Figure 3.5: Technical design of VFM.

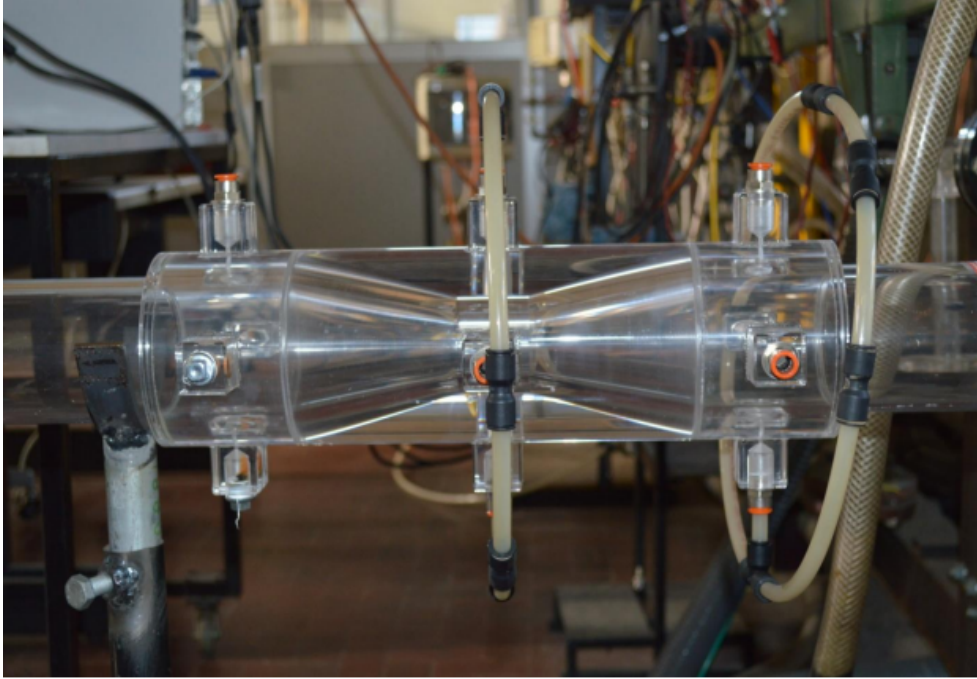


Figure 3.6: Picture of VFM

In the previous experimental campaigns [11], the behavior of the instrument in single-phase flow with air (Fig.3.7) was analyzed to derive the discharge coefficient (C). The single-phase air coefficient was calculated based on the experimental measurements of flow rate and differential pressure:

$$Q = \left[C \cdot A_2 \sqrt{\frac{2 \cdot \Delta p}{\rho \cdot (1 - \beta^4)}} \right] \cdot F_a \cdot Y \quad (3.1)$$

where:

- Q is the volumetric flow;
- C is the discharge coefficient;
- A_2 is the minimal cross section area;
- $\Delta p = p_1 - p_2$ different of pressure between inlet and throat;
- β density;

Considering, using a conservative approach, F_a (thermal expansion correction factor) and Y (compressibility coefficient) equal to 1:

$$C = \frac{Q}{F_a \cdot Y \cdot A_2} \cdot \left(\frac{\rho \cdot (1 - \beta^4)}{2 \cdot \Delta p} \right)^{0.5} \quad (3.2)$$

The dependence on the Reynolds number can be approximated by this law (Fig.3.8):

$$C = a \cdot Re^b, Re = \frac{\rho \cdot V \cdot D}{\mu} \quad (3.3)$$

where the parameters a and b are obtained from experimental calibrations (a=1.5054 and b=-0.0510) and C has a constant value equal to 0.84 for Reynolds numbers greater than $7 \cdot 10^4$.

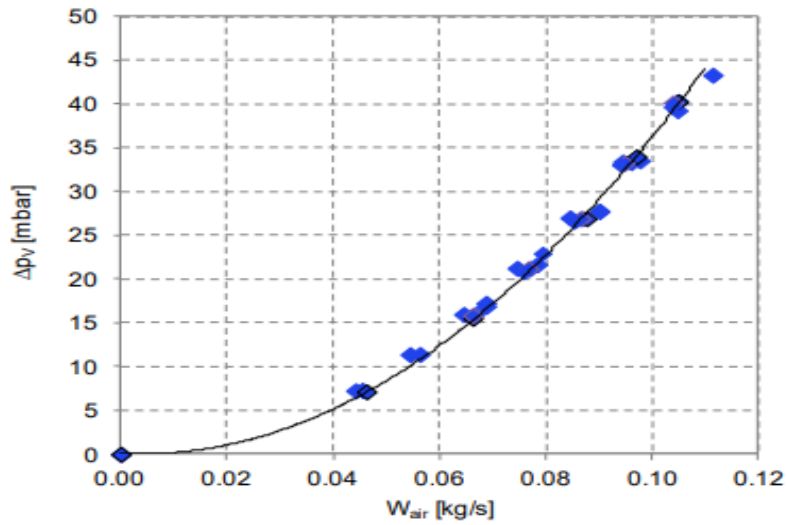


Figure 3.7: Calibration monophase with air of VFM [11].

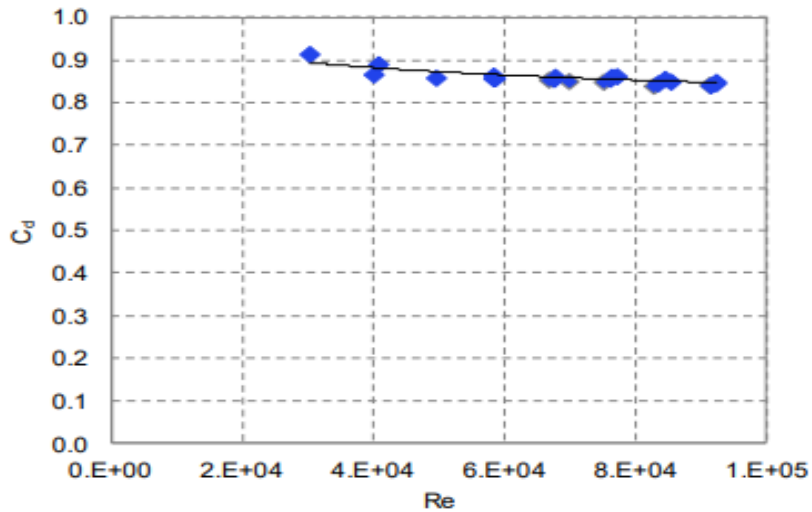


Figure 3.8: Experimental monophase discharge coefficient for VFM [11].

3.3.2 SIET Electrical Capacitance Probe (SIET ECP)

The sensor (ECP), developed by the SIET Company, consists of 10 measurement electrodes: 9 external and 1 internal (Fig.3.9 and Fig.3.10). The internal and the external diameters of the Plexiglas pipe, where the probe is mounted, are 80 mm and 90 mm respectively. The external electrodes (steel stripes of 400 mm length and 5 mm width) are spaced with 22.5 angle only on a half-circumference of the pipe. The angle corresponds to an external chord of 17.56 mm and an internal chord of 15.6 mm. The external electrodes are pasted on the Plexiglas pipe and are welded with the conductor that allows the link with the electronic part; while the internal electrode is connected through a metallic support at the outside of the pipe.

The electrodes are connected in an electronic circuit (Fig.3.11) by several reed relays and two insulation transformers that prevent common mode disturbances. The reed relays technology has been selected for their simplicity and their features: very small electrical capacity and long life. Each external electrode is connected, at the upper and lower extremity, to two reed relays to activate, in a predefined sequence, the excited electrode and the measuring one; the internal one is connected only in the upper extremity and it is always used as measuring electrode, when the corresponding reed relay is activated [19].

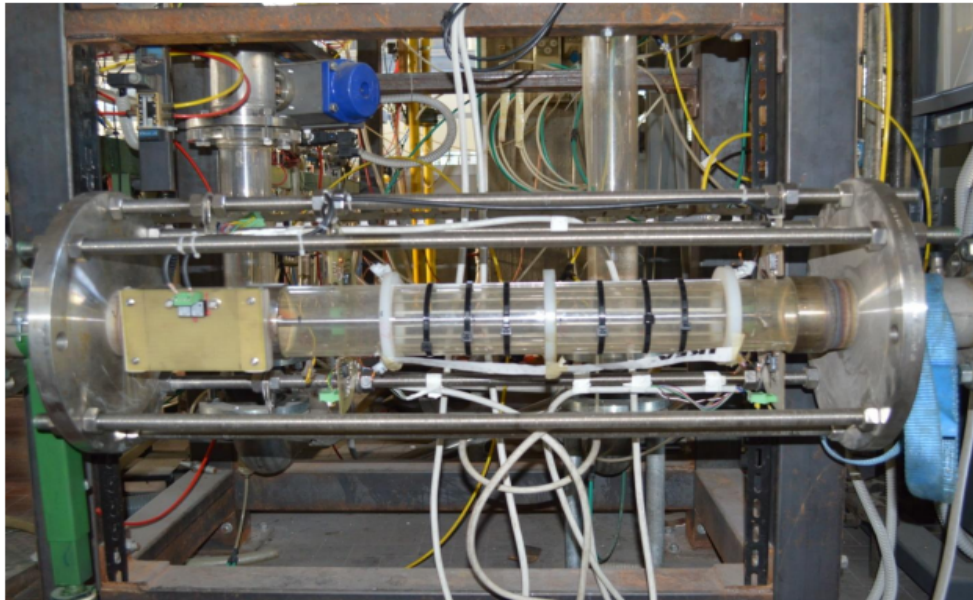


Figure 3.9: Picture of the probe.

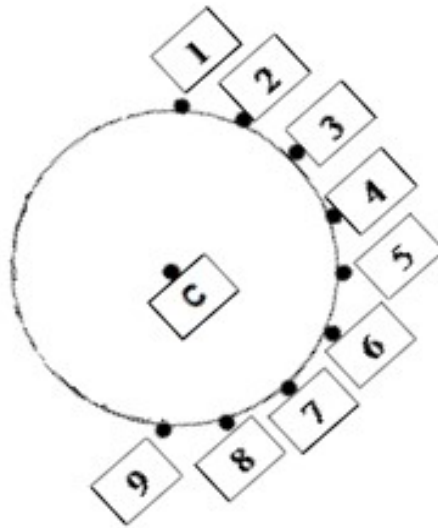


Figure 3.10: Position of the electrodes in the probe.

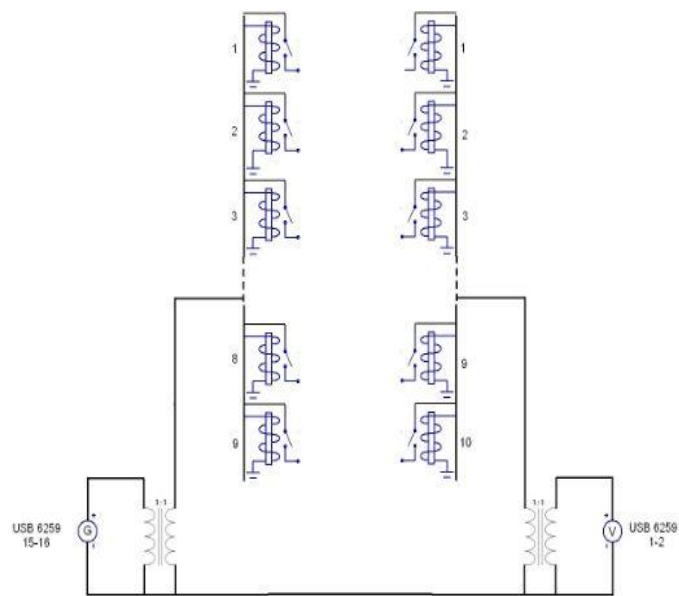


Figure 3.11: Schematic of the probe electronic [19].

The SIET ECP did not provide the average void fraction in the test section but the average linear void fraction along 9 different radii and all the possible cords between the different circumferential electrodes.

Experimental methodology and signal acquisition

As already mentioned, the signals from the sensor are acquired using the NI 6353 DAQ, and managed using a Labview program. The predefined measurement sequence is read and the corresponding reed relay is activated by using a 5V DC signal. The excitation signal is sent to the electrodes (sinusoidal signal with $f=25$ kHz and 5 V amplitude) and the output signal is sampled using a frequency of 250 kHz; the RMS value corresponding to 2000 samples is acquired. The measurement sequence is defined as follows. Before each set of experimental runs the statistic values of the signals for air and water are measured. Then, for each run, the mass flow rates of water and air are fixed and when the flow is stabilized in the test section, the pressure value and the signal from the sensor are acquired. The external electrodes are excited in sequence and for each one the output signal of the other external electrodes is read. After the scan of the external electrodes, the output signal relative to the central electrode is acquired for each excited external electrode. For each measurement cycle all the 81 possible combinations identified by numerical codes (Fig.3.12) are then registered and for each experimental run 100 cycles are acquired, in order to evaluate the mean signal and its time variation.

The signals associated with each pair of electrodes, used to estimate the average linear void fraction, are represented by the RMS value of the potential difference acquired between the two high frequency electrodes.

Each signal is normalized considering the signals associated with all liquid V_L and all vapour V_V , knowing the temperature dependency [20]. Therefore, fixed the pair of electrodes (i, j), the functions are:

$$V_{L,i,j}(T) = V_L(T) \quad (3.4)$$

$$V_{V,i,j}(T) = V_V(T) \quad (3.5)$$

and with a two-phase flow the normalize value:

$$V^*(\alpha, d, T) = \frac{V - V_L}{V_V - V_L} \quad (3.6)$$

where α is the void fraction, d is the circumferential distance between the electrode pair. The electrode pairs with the same circumferential distance d are considered homologous. The normalized value V^* is one in the presence of all liquid and zero in the presence of all gas.

		ECCITANTE								
		1	2	3	4	5	6	7	8	9
ricevente	1	513	514	516	520	528	544	576	640	768
	2	1025	1026	1028	1032	1040	1056	1088	1152	1280
	3	2049	2050	2052	2056	2064	2080	2112	2176	2304
	4	4097	4098	4100	4104	4112	4128	4160	4224	4352
	5	8193	8194	8196	8200	8208	8224	8256	8320	8448
	6	16385	16386	16388	16392	16400	16416	16448	16512	16640
	7	32769	32770	32772	32776	32784	32800	32832	32896	33024
	8	65537	65538	65540	65544	65552	65568	65600	65664	65792
	9	131073	131074	131076	131080	131088	131104	131136	131200	131328
	10	262145	262146	262148	262152	262160	262176	262208	262272	262400

Figure 3.12: Numerical codes that identify electrodes.

3.3.3 DENERG Electrical Capacitance Probe (DENERG ECP)

It is necessary to understand the theory of the capacitance sensor technique to properly optimize and design the sensor of the electrical capacitance probe (ECP).

Applying an external field across the two plates, the charged molecules align themselves with the electric field and produces dipoles with the positive charges in the direction of the applied field and negative charges oppose the field. A dielectric material, containing charged molecules randomly oriented, placed between two conductor plates increase the charge storage capabilities. So, the capacitance measured by a transducer for two-phase flow can be treated as an approximation of a parallel or series combination of capacitors with different dielectric constants. In this way the output signal can be mathematically represent as a function of the void fraction. The relationship between the capacitance and the void fraction depends on the dielectric values of the two phases, the cross-sectional area of the sensors and separation distance between the two electrodes.

The new capacitance probe is made by concave electrodes. Two configuration of concave electrodes with different surfaces, placed on the outer wall of the pipe, made of copper are analysed and shown in Fig.3.13.

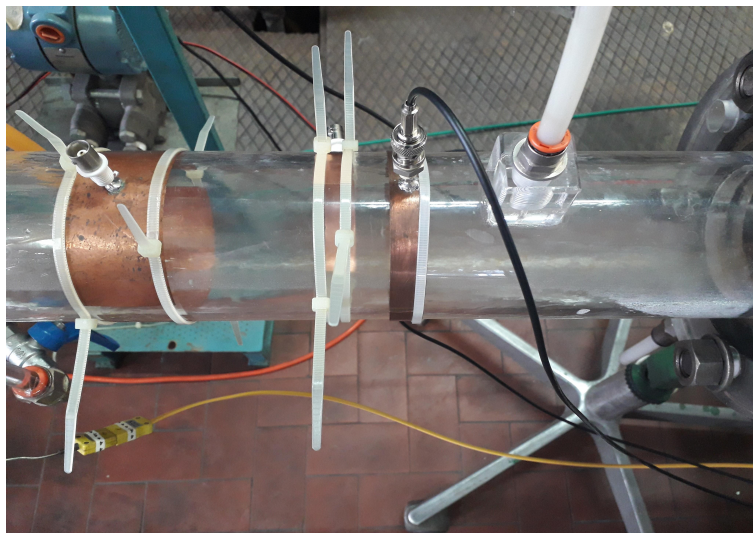


Figure 3.13: Picture of concave electrodes' sensor.

The geometric parameters, schematized in Fig. 3.14 , are shown in Tab 3.6 :

Electrodes	D_e [mm]	D [mm]	L [mm]	g [mm]	w [mm]	S [mm ²]
A	90	80	45	20	125	5625
B	90	80	15	5	140	2100

Table 3.6: Parameters of concave electrodes.

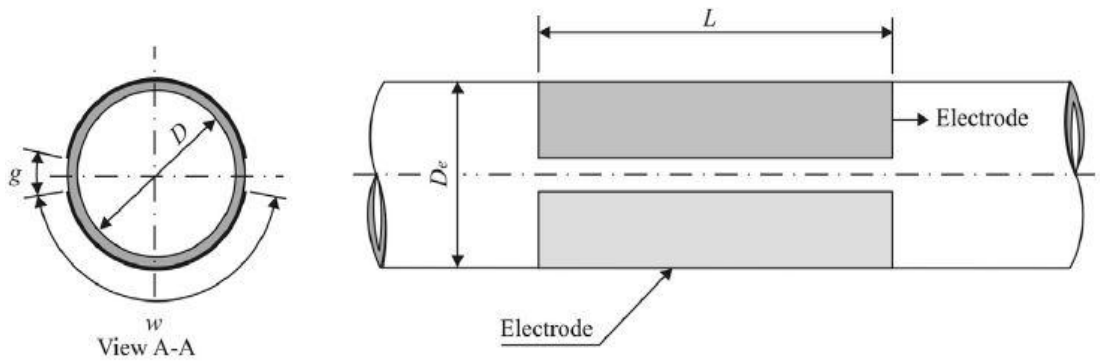


Figure 3.14: Schematic of the concave electrodes' sensor. [2]

In the case of the wider electrodes the signals of the capacitance measured are out of the measurement range. For this reason, it is necessary to design properly the electrodes to optimize the capacitance sensor.

Experimental methodology and signal acquisition

A 24-Bit Capacitance-to-Digital Converter AD7746 (range: $\pm 4\text{pF}$) [17] generates the signal on one concave electrode and receive the response in the other one. These signals are managed by an Evolution Software v2.2 [18]. Before each set of experimental runs the statistic value of the signals for air and water are measured.

Chapter 4

Experimental campaign

4.1 Single-phase calibration

4.1.1 Calibration of the orifice and VFM

The first step is the characterization of the orifice and VFM, varying the frequency of the fun with the inverter, for the single-phase condition.

The geometric and functional characteristics of VFM are shown in table 4.1:

Parameter	Value	Units
diameter D	80.0	<i>mm</i>
area A	0.00502654	<i>m</i> ²
minimum cross-sectional diameter d	40	<i>mm</i>
cross section area Ad	0.001257	<i>m</i> ²
$\vartheta_{convergent} = \vartheta_{divergent}$	21	°
L_{tot}	340	<i>mm</i>
$L_{upstream}$	628	<i>mm</i>
$L_{downstream}$	628	<i>mm</i>

Table 4.1: Parameters of the VFM

Instead, the geometric characteristics of the orifice are shown in table 4.2:

Parameter	Value	Units
diameter D	65.0	mm
area A	0.0033185	m ²
minimum cross-sectional diameter d	30.193	mm
discharge coefficient Cd	0.605	–
characteristic coefficient K	0.000444	m ²

Table 4.2: Parameters of the orifice

Table 4.3 and 4.4 show the results in physical quantities, electric signals generated by the measuring chains already converted:

f [Hz]	$T_{in,air}$ [°C]	$T_{in,probe}$ [°C]	$T_{in,venturi}$ [°C]
10	23.3	22.2	21.5
15	24.5	23.3	22.7
20	27.4	25.9	25
25	28.9	26.6	25.3
30	35.9	33.5	31.6
35	44.5	41.7	39.6
40	52.2	48.9	46.4
45	60.7	53.0	50.6
50	63.3	57.9	53.4

Table 4.3: Temperatures evaluated during single-phase tests with only air.

f [Hz]	$\Delta p_{venturi}$ [mbar]	$\Delta p_{venturi,irr}$ [mbar]	$\Delta p_{orifice}$ [mbar]
10	0	0.887	12.313
15	0.722	1.513	28.205
20	3.387	1.825	50.631
25	6.824	2.732	79.628
30	11.106	4.013	115.079
35	15.747	6.201	152.079
40	21.353	9.327	197.565
45	27.427	12.077	245.799
50	35.054	16.203	307.536

Table 4.4: Differential pressure drops evaluated during single-phase tests with only air.

The air mass flow rate flowing through the orifice is estimated (Table 4.5), based on the differential pressure of the orifice, with the following formula:

$$Q_{m,a} = C \cdot \sqrt{2 \cdot \rho_g \cdot \Delta p} \quad (4.1)$$

with ρ_g function of pressure and temperature in $[kg/m^3]$, Δp in Pa and $C=0.00044 m^2$.

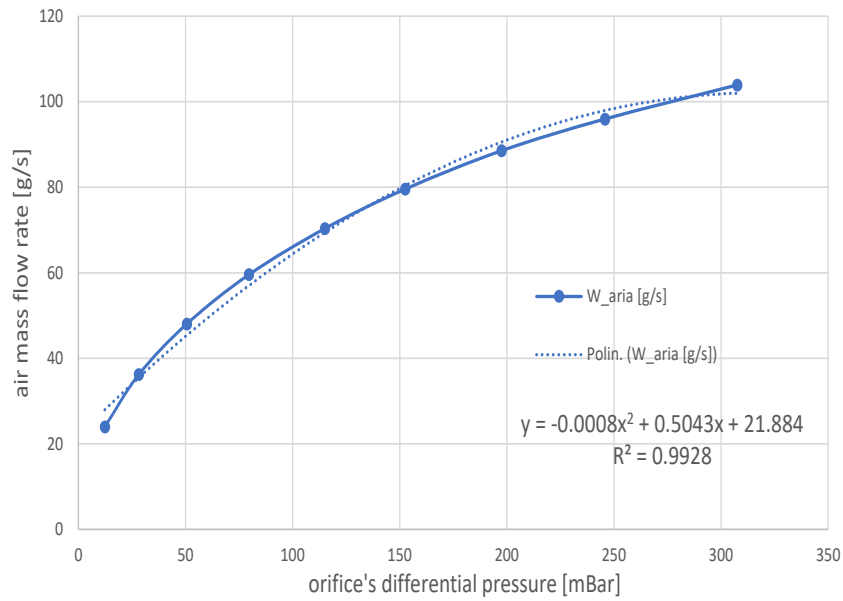


Figure 4.1: Calibration curve for the evaluation of the air mass flow.

$f [Hz]$	$W_{air} [g/s]$
10	23.96
15	36.21
20	48.04
25	59.57
30	70.34
35	79.55
40	88.54
45	95.95
50	103.91

Table 4.5: Air mass flow rate varying the frequency.

The Fig. 4.2 shows the parabolic trends of the differential pressures of the orifice and Venturi. It's interesting to note how the single-phase flow rate, delivered by the fan, varies with approximately linear law with the frequency of the inverter.

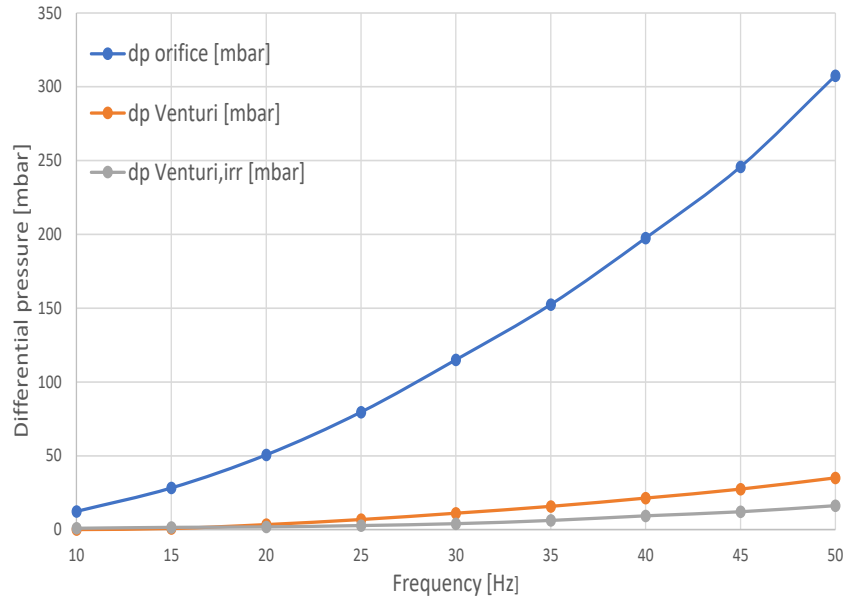


Figure 4.2: Differential pressure measured in the orifice and in VFM varying the frequency.

The air circuit isn't equipped with a cooling exchanger; therefore, as the frequency of the inverter which regulates the fan increases (increasing of air mass flow), the temperature of the fluid increases considerably. Fig. 4.3 shows that for the single-phase air tests the temperature increase is conserved in the test section, even though a relatively small temperature decrease (3-10 °C) is observed along the test section. In the two-phase tests, on the contrary (Fig. 4.4), the temperature is considerably reduced by the injection of the cold water.

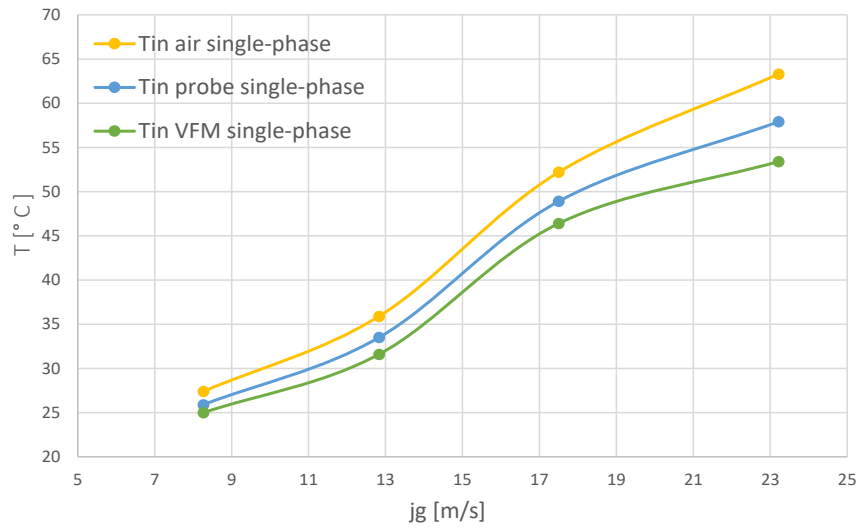


Figure 4.3: Temperature along the test section versus air superficial velocity-single-phase.

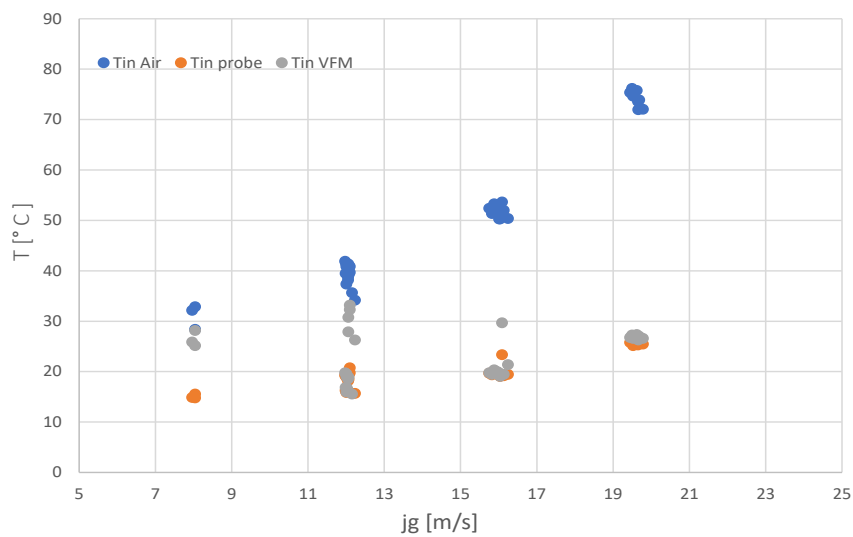


Figure 4.4: Temperature along the test section versus air superficial velocity-two-phase.

4.1.2 Calibration of ECPs

All the ECPs have been calibrated in static conditions in order to characterize their output signal with liquid only, air only and known heights of water in the test section. In each run, the water and air mass flow rates are regulated respectively by changing the frequency of the inverter connected to the blower and by opening/closing a needle valve located downstream the rotameter. Since the water is provided by gravity and the water tank is located just 3 m above the test section, the possible operational range is not too wide due to the limited available gravitational head. Pressures, temperatures and the signals from the probes are acquired when the flow in the test section has reached steady-state conditions.

Calibration of the SIET ECP

Through the response of the probe in static single-phase conditions with air and demineralized water, the range of the measurements and the sensitivity of the instrument are established. The angular distance is counted starting from the electrode 1 positioned on the top of the horizontal probe while the electrode 9 is positioned on the bottom.

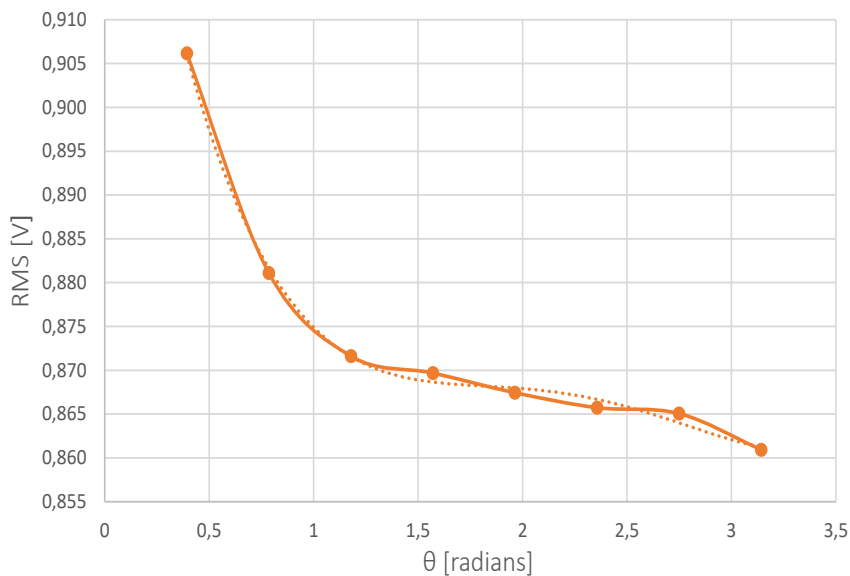


Figure 4.5: RMS values function of the angular distance, case with air.

coefficients	a0	a1	a2	a3	a4	R2
values	0.0036	-0.0337	0.1113	-0.16	0.9536	0.9974

Table 4.6: Polynomial coefficients of best fit (4-degree) case single-phase with air.

Fig. 4.5 and 4.6 show the RMS values (Root Mean Square) obtained exciting the electrode 1 and measuring the electrical voltage associated with the other electrodes function of the angular distance for air and demineralized water. Dashed curves represent the polynomials of the best fit curve. So , the equation of the best fitting curve in the case with air is:

$$y = 0.036x^4 - 0.0337x^3 + 0.1113x^2 - 0.16x + 0.9536 \quad (4.2)$$

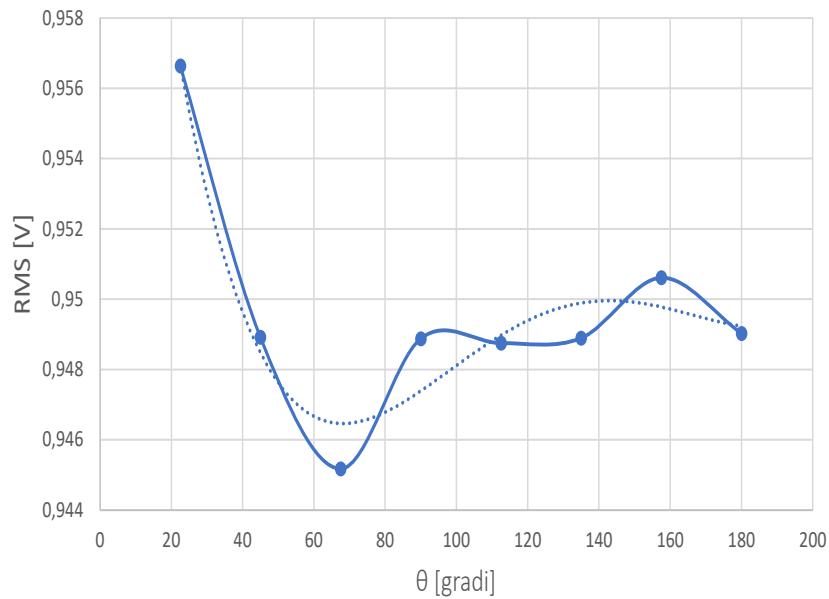


Figure 4.6: RMS values function of the angular distance, case with water.

coefficients	a0	a1	a2	a3	a4	R2
values	0.0017	-0.0155	0.0502	-0.0648	0.9753	0.9195

Table 4.7: Polynomial coefficients of best fit (4-degree) case single-phase with demineralized water.

So , the equation of the best fitting curve in the case of water is:

$$y = 0.0017x^4 - 0.0155x^3 + 0.0502x^2 - 0.0648x + 0.9753 \quad (4.3)$$

RMS_{water}/RMS_{air} is a value between 1.05 and 1.11 function of the angle θ . The central electrode, in direct contact with the fluid, undergoes the attenuation of a single layer of plexiglass and for this reason the signal relative to each test is calculated as the arithmetic mean of the 9 signals of the external electrodes. In this case, RMS_{water}/RMS_{air} is a value between 1.71 and 1.72 function of the angle θ .

The reference values for signal normalization are shown in Fig. 4.7 (exciting electrode 1) and Fig. 4.8 (exciting electrode 9) where the two curves obtained with air and water are shown together.

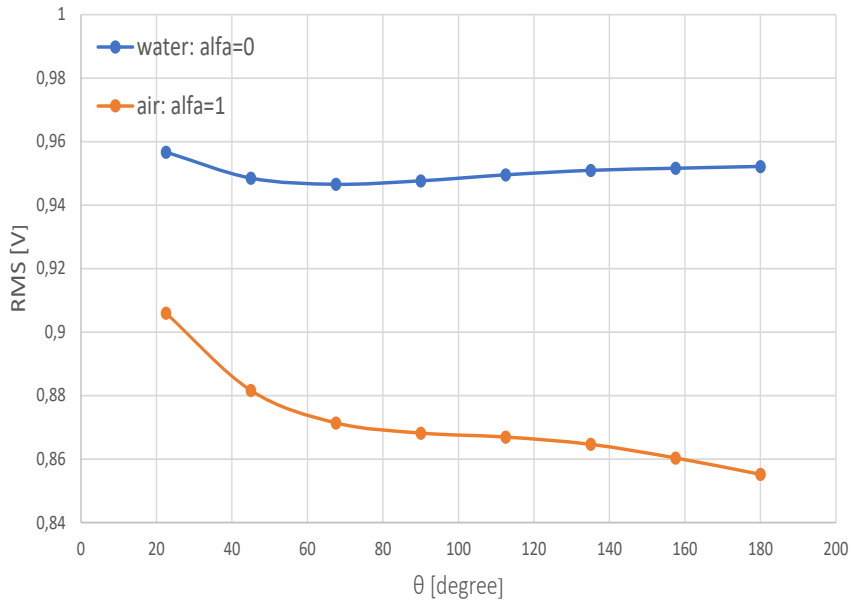


Figure 4.7: RMS values function of the angular distance (exciting electrode 1).

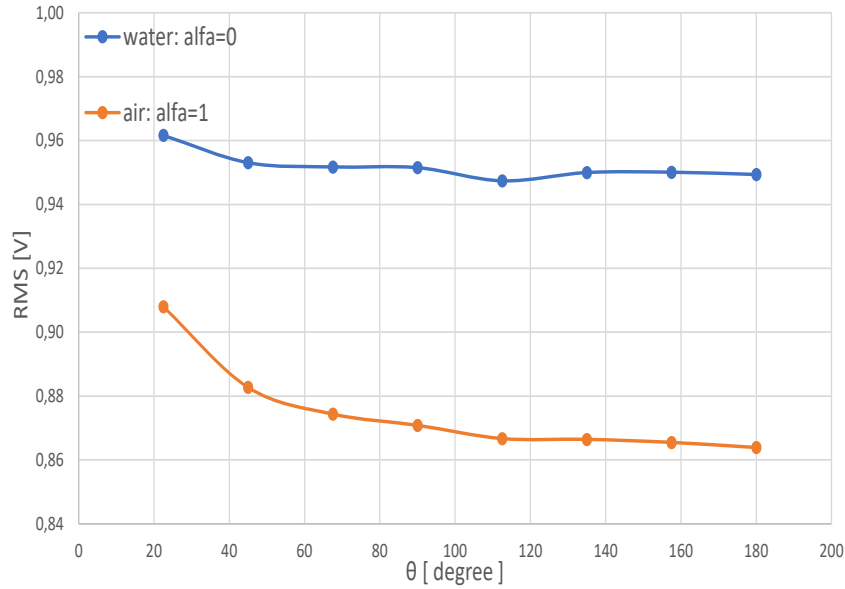


Figure 4.8: RMS values function of the angular distance (exciting electrode 9.)

In the static tests the quick isolation valves are closed and a level of water is imposed in the test section. The horizontal pipe is filled gradually with demineralized water to cover the various electrodes, realizing a stratified regime typical of horizontal flows.

Signals, characterized in term of RMS and standard deviations, are obtained exciting an electrode and measuring the electric voltage associated with all the other electrodes.

The aim is to characterize the response signals of the probe with functions:

$$S_{e,r} = f(\theta_e, \theta_r, \alpha) \quad (4.4)$$

where:

- θ_e is the angle of the excitation electrode;
- θ_r is the angle of the receiving electrode;
- α is the void fraction

Knowing that R is the internal radius of the pipe, θ is the semi-angle of the circular segment occupied by water and h the height, the area occupied by

the circular segment, the level of water and the void fraction are described by the following formulas (Fig. 4.9):

$$A = \frac{1}{2}R^2 \cdot [2\theta - \sin(2\theta)] \quad (4.5)$$

$$h = R \cdot (1 - \cos(\theta)) \quad (4.6)$$

$$\alpha = \frac{A_{tot} - A}{A_{tot}} \quad (4.7)$$

where A_{tot} is the total area of the circular sector. The table 4.8 shows the results of the 7 tests in static regime of single-phase water flow.

test	angle [°]	level _{estimated} [mm]	α [-]	level _{experimental} [mm]
2 "ele"	22.5	3.0	0.99	3.0
3 "ele"	45	11.7	0.91	11.3
4 "ele"	67.5	24.7	0.74	23.7
5 "ele"	90	40.0	0.5	41.3
6 "ele"	112.5	55.3	0.26	56.7
7 "ele"	135	68.3	0.09	69.6
9 "ele"	180	80	0.0	80

Table 4.8: ECP probe: static test conditions.

The legend "2ele" means that the water level covered respectively 2 electrodes (starting from the bottom of the pipe), electrodes 9 and 8; "3ele" that the water level covered electrodes 9,8,7 etc.. until you get to "9ele" pipe completely full of water.

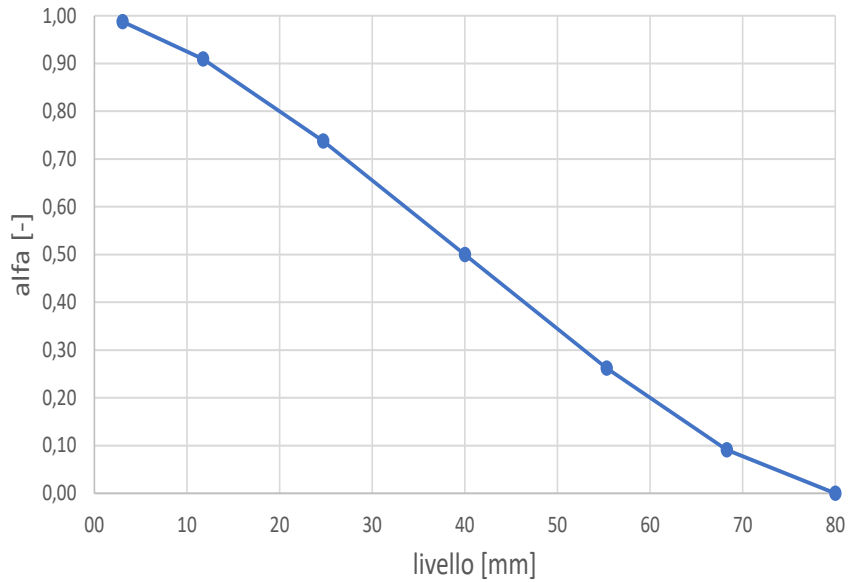


Figure 4.9: alpha trend as a function of the level.

Fig. 4.10 and Fig. 4.11 show signal variation for pairs 1-9 depending on the angle.

Fig. 4.10 show that when the pipe is completely filled with demineralized water, the signal shows the dependence on the distance between the electrodes. Instead, in the case of lower water heights the measurement depends on both the angle and the conduit fraction occupied by the liquid level.

Electrode 9 (Fig. 4.11) is always covered by water so the measurements, varying the distance, show a clear dependence of the signal on the height of the water in the pipe.

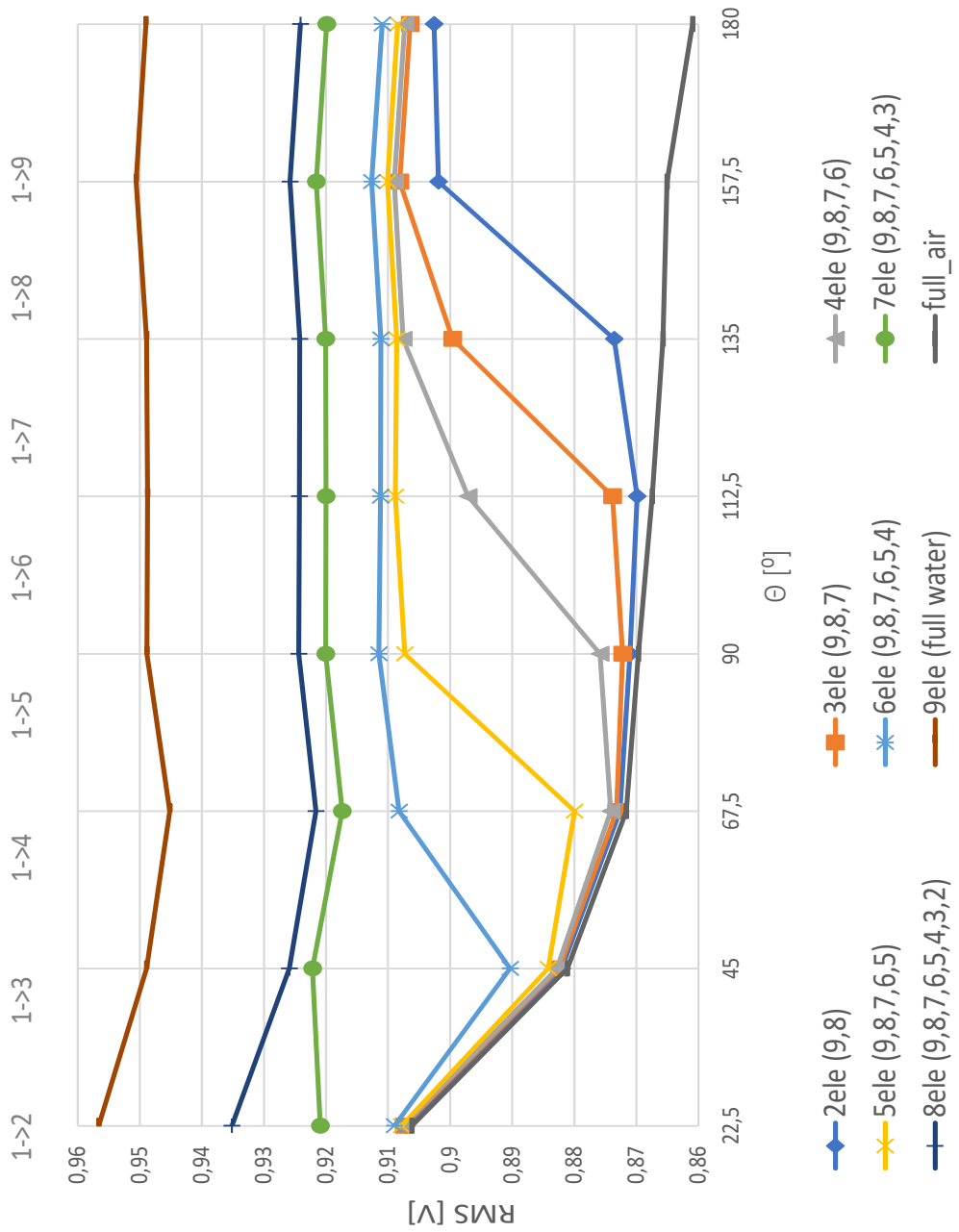


Figure 4.10: Signals (electrode exciting: 1, receiving electrodes 2:9) function of the angle for different levels of water of the circuit.

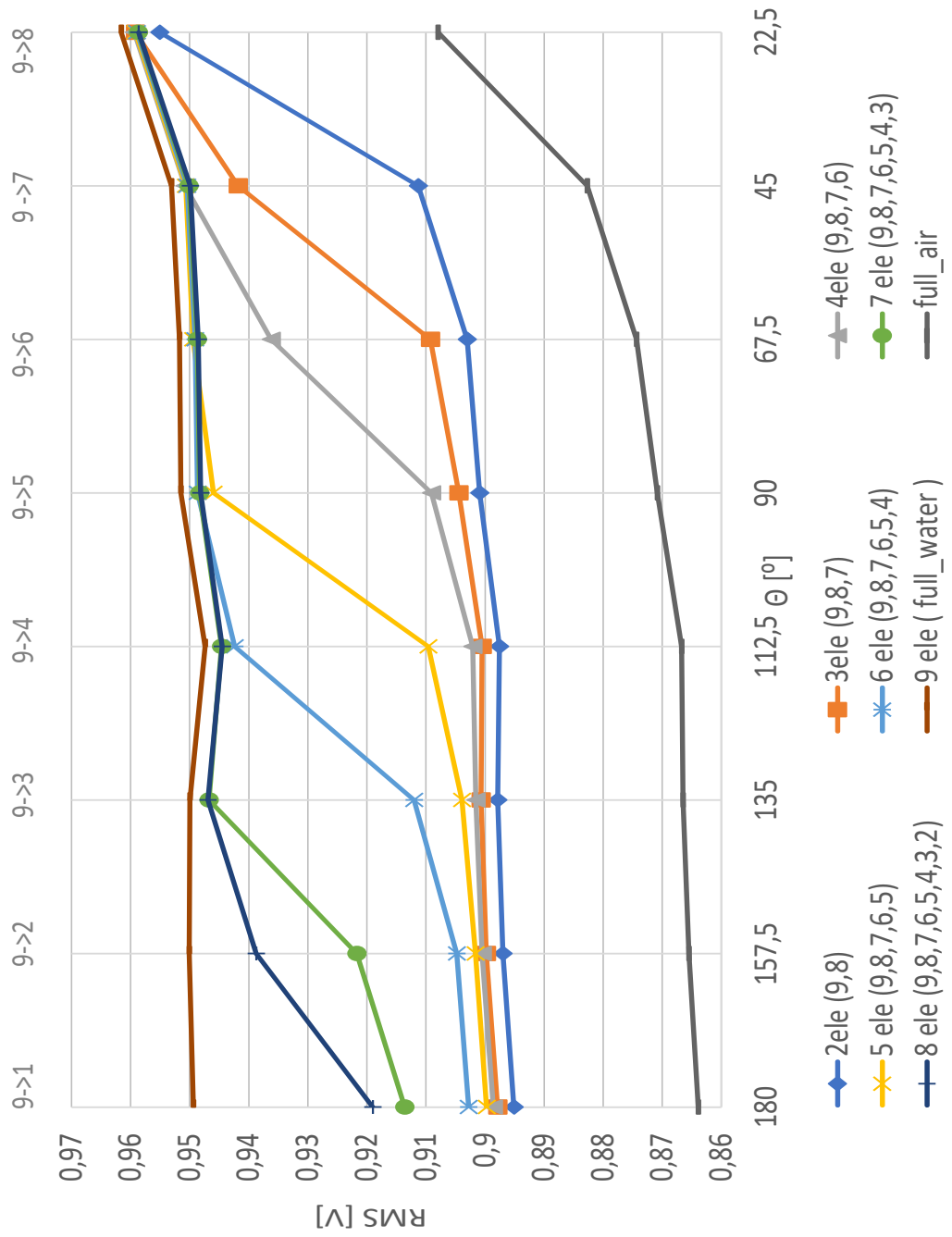


Figure 4.11: Signals (electrode exciting: 9, receiving electrodes 1:8) function of the angle for different levels of water of the circuit.

Calibration of the DENERG ECP

To perform the static calibration of the new Electric Capacitance Probes with concave electrodes developed at DENERG (geometric parameters in Tab. 4.9), the quick isolation valves have been closed, the test section has been gradually filled and the relationships between the equivalent electrical capacitance of the water-air mixture and the water level in the probe was found. These relationships are represented in Figure 4.12 and 4.13.

In presence of a mixture of air and water, the probes behaves as capacitors in series with different dielectric constants, and they show a good sensitivity at low liquid level (level lower than the half pipe).

Electrodes	D_e [mm]	D [mm]	L [mm]	g [mm]	w [mm]	S [mm ²]
A	90	80	45	20	125	5625
B	90	80	15	5	140	2100

Table 4.9: Parameters of concave electrodes.

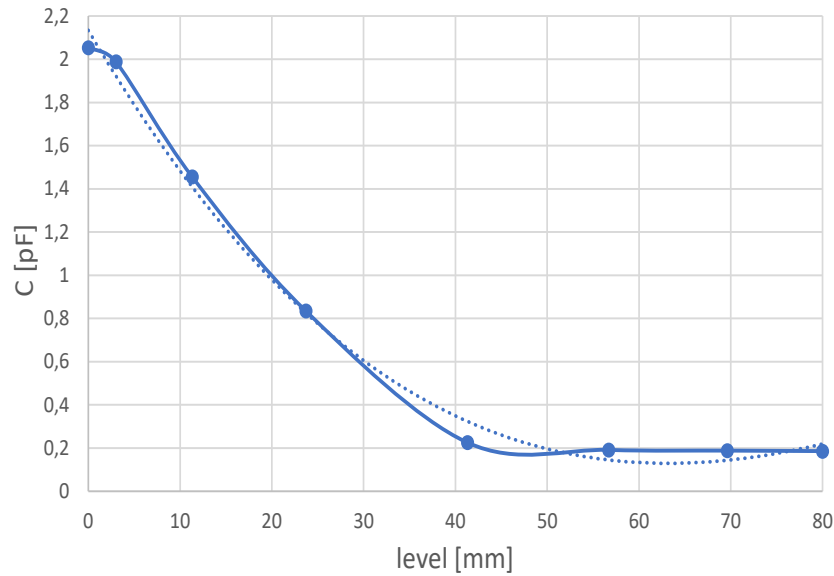


Figure 4.12: Calibration of the configuration A of the concave electrodes' sensor.

where the dashed line represent the best fit curve, given by the following

equation:

$$C = 0.0005l^2 - 0.0646l + 2.1039 \quad (4.8)$$

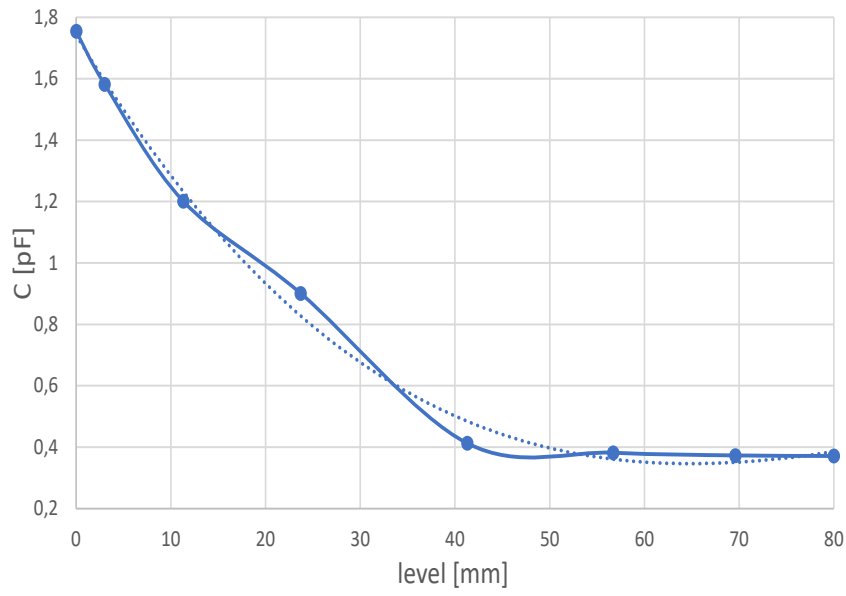


Figure 4.13: Calibration of the configuration B of the concave electrodes' sensor.

where the dashed line represent the best fit curve, given by the following equation:

$$C = 0.0004l^2 - 0.0445l + 1.7171 \quad (4.9)$$

4.2 Experimental flow pattern with Taitel-Duckler map

The transparent pipes of the test section allowed to visualize the evolution of the flow pattern along the pipe. In all the experimental tests stratified-wavy and dispersed-annular flow patterns occurred along the first part of the test section, i.e. from the inlet of the test section up to the inlet of the VFM. The VFM perturbs the flow pattern, which converts to dispersed flow downstream the VFM in all the experimental tests. The experimental flow pattern along the first part of the test section have been compared with the Taitel-Duckler map for horizontal flow.

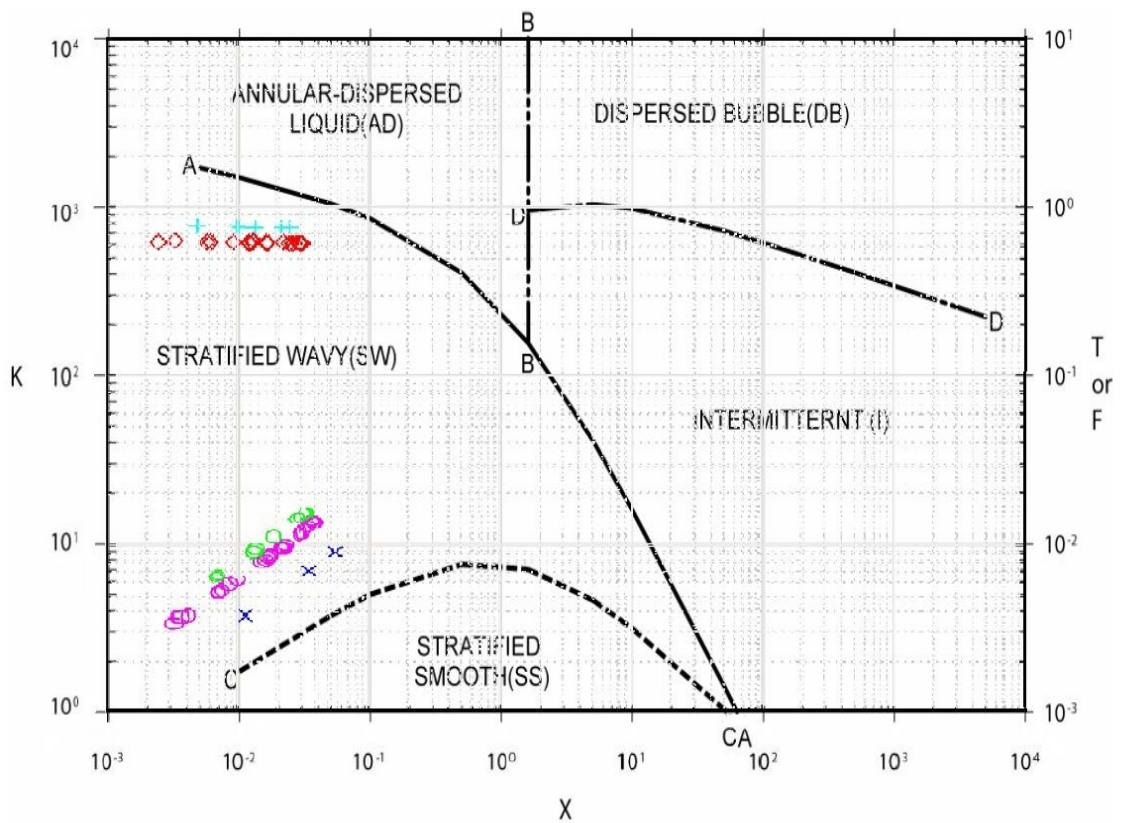


Figure 4.14: Data of the experimental campaign in Taitel and Duckler's map.

In the map in Fig. 4.14 are shown some of the data of the experimental campaign carried out in this thesis work. For the same range of the water mass flow rate (between 0.003 kg/s and 0.052 kg/s) five data sets are shown:

- blue x with an air flow rate of 0.048 kg/s (20Hz);

- pink circles with an air flow rate of 0.070 kg/s (30Hz);
- green circles with an air flow rate of 0.079 kg/s (35Hz);
- red diamonds with an air flow rate equal to 0.088 kg/s (40Hz);
- light blue x with an air flow rate equal to 0.104 kg/s (50Hz).

The flow pattern boundaries are not distinctive lines but just transition zones.

The agreement is good in the experimental runs with lower value of the air superficial velocity, since the flow pattern in this region is still developing; in fact the length to diameter ratio at the VFM entrance is approximately equal to 25. Downstream the VFM, the length of the pipe is 450 mm only, which corresponds to L/D equal to 5.6; therefore the flow pattern is still fully undeveloped and cannot be compared with any flow pattern map or model.

4.3 Two-phase tests

The parameters provided by the VFM and the probes are the following:

- differential pressure between inlet and throat section of Venturi;
- differential pressure between inlet and outlet section of Venturi;
- operating temperature;
- operating pressure;
- RMS voltage between pairs of electrodes in the ECP;
- Capacitance between concave electrodes' sensor.

For the present experimental campaign, the flow rates' range is 0.048 – 0.0119 kg/s for air (superficial velocity range 8-19 m/s) and 0 – 0.0535 kg/s (0-192 l/h) for water (superficial velocity's range 0.0006 – 0.0103 m/s). The experimental void fraction's range is 0.976-0.997 and flow quality's range 0.60-0.96. For the same couple of flow rates of the liquid and gas phases several tests have been carried out to assess the repeatability of the measurements.

The following tables shows the experimental matrix: frequency of the inverter, flow rate for the gas and liquid phases, total flow rate, flow quality x, superficial velocity of the gas phase and superficial velocity of the liquid

phase.

test	$f_{inverter}$ [Hz]	W_g [kg/s]	W_l [kg/s]	W_{tot} [kg/s]
1	20	0.0486	0.091	0.0577
2	20	0.0481	0.0330	0.0811
3	20	0.0486	0.05	0.1027

test	x [-]	j_g [m/s]	j_l [m/s]
1	0.8426	8.0378	0.0018
2	0.5936	7.9580	0.0066
3	0.4729	8.0355	0.0108

Table 4.10: Experimental matrix in two phase flow tests with $f_{inverter} = 20Hz$.

test	$f_{inverter}$ [Hz]	W_g [kg/s]	W_l [kg/s]	W_{tot} [kg/s]
4	30	0.0728	0.0034	0.0762
5	30	0.0730	0.0039	0.0769
6	30	0.0726	0.0085	0.0811
7	30	0.0727	0.0098	0.0826
8	30	0.0726	0.0207	0.0933
9	30	0.0725	0.0211	0.0936
10	30	0.0724	0.0268	0.0992
11	30	0.0723	0.0270	0.0993
12	30	0.0723	0.0292	0.1015
13	30	0.0719	0.0385	0.1104
14	30	0.0727	0.0390	0.1118
15	30	0.0726	0.0480	0.1206
16	30	0.0727	0.0520	0.1248
17	30	0.0735	0.0218	0.0953
18	30	0.0741	0.0038	0.0799
19	30	0.0730	0.0524	0.1254
20	30	0.0717	0.0042	0.0759
21	30	0.0709	0.0114	0.0823
22	30	0.0714	0.0272	0.0986
23	30	0.0725	0.0080	0.0805
24	30	0.0720	0.0185	0.0905
25	30	0.0717	0.0273	0.0990
26	30	0.0714	0.0437	0.1151
27	30	0.0712	0.0534	0.1246
28	30	0.0721	0.0079	0.0800
29	30	0.0718	0.0196	0.0914
30	30	0.0713	0.0407	0.1121
31	30	0.0715	0.0273	0.0989
32	30	0.0709	0.0535	0.1245

Table 4.11: Experimental matrix in two phase flow tests with $f_{inverter} = 30Hz$.

test	x [-]	j_g [m/s]	j_l [m/s]
4	0.9560	12.0906	0.0007
5	0.9496	12.0912	0.0008
6	0.8949	12.0527	0.0017
7	0.8807	12.0524	0.0020
8	0.7786	12.0445	0.0041
9	0.7745	12.0608	0.0042
10	0.7297	12.0047	0.0054
11	0.7279	12.0047	0.0054
12	0.7119	12.0067	0.0058
13	0.6514	11.9698	0.0077
14	0.6509	12.0169	0.0078
15	0.6018	11.9849	0.0096
16	0.5829	11.9988	0.0014
17	0.7710	12.1508	0.0044
18	0.9511	12.2261	0.0008
19	0.5819	12.0457	0.0105
20	0.9441	11.9468	0.0008
21	0.8619	11.8319	0.0023
22	0.7245	11.9244	0.0054
23	0.9009	12.0579	0.0016
24	0.7959	11.9798	0.0037
25	0.7244	11.9297	0.0054
26	0.6205	11.8866	0.0087
27	0.5716	11.8606	0.0106
28	0.9014	11.9968	0.0016
29	0.7857	11.9467	0.0039
30	0.6366	11.8786	0.0081
31	0.7234	11.9107	0.0055
32	0.5699	11.8175	0.0107

Table 4.12: Experimental matrix in two phase flow tests with $f_{inverter} = 30Hz$.

test	$f_{inverter}$ [Hz]	W_g [kg/s]	W_l [kg/s]	W_{tot} [kg/s]
33	32	0.0761	0.0520	0.1281
34	32	0.0761	0.0436	0.1198
35	32	0.0763	0.0270	0.1034
36	32	0.0766	0.0177	0.0943
37	32	0.0767	0.0091	0.0858
38	32	0.0761	0.0526	0.1287
39	32	0.0763	0.0415	0.1178
40	32	0.0764	0.0268	0.1033
41	32	0.0767	0.0178	0.0945
42	32	0.0769	0.0083	0.0852
43	33	0.0798	0.0089	0.0887
44	33	0.0792	0.0190	0.0982
45	33	0.0761	0.0268	0.1029
46	33	0.0785	0.0440	0.1225
47	33	0.0797	0.0528	0.1325
48	34	0.0817	0.0083	0.0901
49	34	0.0814	0.0188	0.1001
50	34	0.0811	0.0273	0.1084
51	34	0.0808	0.0450	0.1258
52	34	0.0806	0.0526	0.1332
53	35	0.0847	0.0092	0.0939
54	35	0.0841	0.0193	0.1033
55	35	0.0837	0.0269	0.1106
56	35	0.0834	0.0426	0.1260
57	35	0.0831	0.0531	0.1344
58	35	0.0841	0.0088	0.0929
59	35	0.0838	0.0180	0.1018
60	35	0.0834	0.0268	0.1102
61	35	0.0831	0.0454	0.1285
62	35	0.0830	0.0517	0.1347
63	36	0.0868	0.0084	0.0952
64	36	0.0861	0.0189	0.1050
65	36	0.0857	0.0268	0.1124
66	36	0.0854	0.0428	0.1282
67	36	0.0852	0.0516	0.1368
68	37	0.0885	0.0086	0.0972
69	37	0.0882	0.0188	0.1070
70	37	0.0879	0.0268	0.1146
71	37	0.0877	0.0423	0.1299
72	37	0.0875	0.0511	0.1386
73	38	0.0911	0.0083	0.0994
74	38	0.0907	0.0182	0.1089
75	38	0.0904	0.0269	0.1173
76	38	0.0901	0.0430	0.1331
77	38	0.0899	0.0520	0.1419

Table 4.13: Experimental matrix in two phase flow tests with $f_{inverter}$ from 32 to 38 Hz.

test	x [-]	j_g [m/s]	j_l [m/s]
33	0.5940	12.6889	0.0104
34	0.6356	12.7032	0.0087
35	0.7384	12.7426	0.0054
36	0.8122	12.7806	0.0035
37	0.8942	12.8129	0.0018
38	0.5913	12.6746	0.0105
39	0.6476	12.7140	0.0083
40	0.7401	12.7369	0.0054
41	0.8115	12.7842	0.0036
42	0.9025	12.8236	0.0017
43	0.8992	13.3147	0.0018
44	0.8070	13.2338	0.0038
45	0.7398	12.7097	0.0053
46	0.6411	13.1184	0.0088
47	0.6012	13.3164	0.0105
48	0.9075	13.6747	0.0017
49	0.8126	13.6094	0.0037
50	0.7482	13.5619	0.0054
51	0.6423	13.5044	0.0090
52	0.6051	13.4816	0.0105
53	0.9023	14.1304	0.0018
54	0.8135	14.0299	0.0038
55	0.7568	13.9646	0.0054
56	0.6617	13.9168	0.0085
57	0.6181	13.8717	0.0102
58	0.9053	14.0130	0.0018
59	0.8234	13.9652	0.0036
60	0.7569	13.9027	0.0053
61	0.6466	13.8573	0.0091
62	0.6161	13.8372	0.0103
63	0.9118	14.4988	0.0017
64	0.8199	14.3982	0.0038
65	0.7620	14.3155	0.0053
66	0.6660	14.2703	0.0085
67	0.6226	14.2426	0.0103
68	0.9113	14.8275	0.0017
69	0.8241	14.7572	0.0038
70	0.7666	14.6970	0.0053
71	0.6747	14.6618	0.0084
72	0.6314	14.6317	0.0102
73	0.9162	15.2471	0.0017
74	0.8327	15.1767	0.0036
75	0.7709	15.1087	0.0054
76	0.6771	15.0636	0.0086
77	0.6337	15.0309	0.0104

Table 4.14: Experimental matrix in two phase flow tests with $f_{inverter}$ from 32 to 38 Hz.

test	$f_{inverter}$ [Hz]	W_g [kg/s]	W_l [kg/s]	W_{tot} [kg/s]
78	40	0.0966	0.0033	0.0999
79	40	0.0965	0.0089	0.1054
80	40	0.0961	0.0143	0.1104
81	40	0.0958	0.0210	0.1168
82	40	0.0958	0.0268	0.1226
83	40	0.0957	0.0374	0.1331
84	40	0.0952	0.0514	0.1467
85	40	0.0981	0.0044	0.1025
86	40	0.0974	0.0209	0.1183
87	40	0.0969	0.0517	0.1486
88	40	0.0957	0.0093	0.1050
89	40	0.0953	0.0188	0.1141
90	40	0.0949	0.0268	0.1217
91	40	0.0948	0.0430	0.1378
92	40	0.0944	0.0514	0.1458
93	40	0.0961	0.0082	0.1043
94	40	0.0954	0.0193	0.1147
95	40	0.0944	0.0524	0.1468
96	40	0.0947	0.0273	0.1220
97	40	0.0941	0.0454	0.1395
98	40	0.0941	0.0524	0.1465
99	40	0.0943	0.0418	0.1361
100	40	0.0952	0.0091	0.1043
101	40	0.0949	0.0189	0.1138
102	40	0.0946	0.0271	0.1217

Table 4.15: Experimental matrix in two phase flow tests with $f_{inverter} = 40$ Hz.

test	x [-]	j_g [m/s]	j_l [m/s]
78	0.9671	16.0853	0.0007
79	0.9154	16.0030	0.0018
80	0.8707	15.9584	0.0028
81	0.8201	15.9007	0.0042
82	0.7812	15.8749	0.0054
83	0.7190	15.8183	0.0075
84	0.6493	15.7461	0.0103
85	0.9569	16.2415	0.0009
86	0.8236	16.1266	0.0042
87	0.6518	16.0289	0.0103
88	0.9114	16.0237	0.0019
89	0.8350	15.9506	0.0038
90	0.7801	15.8696	0.0053
91	0.6880	15.8341	0.0086
92	0.6477	15.7892	0.0102
93	0.9212	16.0237	0.0016
94	0.8318	15.9137	0.0038
95	0.6429	15.7431	0.0105
96	0.7760	15.8037	0.0054
97	0.6745	15.7133	0.0091
98	0.6424	15.7210	0.0104
99	0.6928	15.7564	0.0083
100	0.9130	15.9225	0.0018
101	0.8340	15.8776	0.0038
102	0.7771	15.8247	0.0054

Table 4.16: Input datas in two phase flow tests with $f_{inverter} = 40Hz$.

test	$f_{inverter}$ [Hz]	W_g [kg/s]	W_l [kg/s]	W_{tot} [kg/s]
103	50	0.1189	0.0086	0.1275
104	50	0.1182	0.0188	0.1370
105	50	0.1174	0.0268	0.1442
106	50	0.1183	0.0084	0.1267
107	50	0.1168	0.0513	0.1680
108	50	0.1178	0.0268	0.1446
109	50	0.1168	0.0457	0.1625
110	50	0.1175	0.0194	0.1369

Table 4.17: Experimental matrix in two phase flow tests with $f_{inverter} = 50Hz$.

test	x [-]	j_g [m/s]	j_l [m/s]
103	0.9328	19.7768	0.0017
104	0.8625	19.6482	0.0038
105	0.8140	19.5213	0.0053
106	0.9337	19.6800	0.0017
107	0.6949	19.4410	0.0102
108	0.8145	19.6514	0.0053
109	0.7188	19.4909	0.0091
110	0.8580	19.6129	0.0039

Table 4.18: Experimental matrix in two phase flow tests with $f_{inverter} = 50Hz$.

The following tables show, for each test, the elaborated signals of temperature, absolute pressure, differential pressure between inlet and throat section and differential pressure between inlet and outlet section of VFM.

test	T_{amb} [$^{\circ}C$]	T_{air} [$^{\circ}C$]	T_{probe} [$^{\circ}C$]	$T_{venturi}$ [$^{\circ}C$]
1	20.1	28.4	14.8	25.2
2	20.1	32.2	14.9	25.9
3	20.3	32.9	15.6	28.2
4	21.3	40.9	20.8	33.2
5	20.6	39.7	19.8	32.3
6	21.4	41.4	19.6	30.8
7	20.9	40.6	19.1	27.9
8	21	38.8	18.2	18.6
9	21.8	39.2	18.5	18.9
10	21	40.9	18.9	19.1
11	21.5	41.4	19.2	19.6
12	21.6	41.3	19.1	19.4
13	22	41.9	19.3	19.8
14	19.9	39.5	16.3	16.8
15	19.8	39.5	16.3	16.9
16	19.5	37.4	15.9	16
17	20.1	35.7	15.7	15.6
18	19.4	34.2	15.7	26.3
19	19.6	38.2	16.2	16.2
20	22.6	40.4	21.9	22.4
21	22.9	42.0	22.1	22.5
22	23.0	41.5	21.8	22.1
23	21.9	36.1	19.6	26.6
24	22.0	40.8	20.6	21.4
25	22	41.8	20.9	21.3
26	22.1	42.8	20.9	21.2
27	22.3	42.4	21	21.4
28	22.1	40.2	21	25
29	22.1	41.3	20.7	21.5
30	22.2	41.9	20.6	21
31	22.3	42.1	20.7	21.1
32	22.4	42.6	20.9	21.3
33	22.6	45	22.2	22.3
34	22.8	45.3	22.4	22.8
35	23	45.4	22.4	22.7
36	22.9	45.4	22.4	23.1
37	23	45.3	22.7	29.5
38	22.4	46.7	22.7	23
39	22.6	45.1	22.4	22.6
40	22.5	45.2	22.4	23.7
41	22.6	45.1	22.3	23
42	22.8	45	22.6	31.2
43	23	41.7	21.2	22.5

Table 4.19: Temperatures in two phase flow tests.

test	T_{amb} [$^{\circ}C$]	T_{air} [$^{\circ}C$]	T_{probe} [$^{\circ}C$]	$T_{venturi}$ [$^{\circ}C$]
44	23.2	45.3	22	22.5
45	23.1	46.2	22.2	22.5
46	23.2	46.5	22.3	22.7
47	23.3	46.8	22.5	22.8
48	23.6	46.1	22.3	25.5
49	23.6	47.7	22.6	23.1
50	23.5	48	22.7	23
51	23.4	48.3	22.9	23
52	23.5	48.4	23	23.2
53	22.7	42.9	21.5	21.8
54	22.9	47.9	22.5	22.9
55	22.9	48.9	22.7	23.1
56	23	49.3	23	23.3
57	23	49.6	23	23.4
58	22.4	47.5	22.2	23.2
59	22.5	48.9	22.4	22.9
60	22.4	49.3	22.5	22.7
61	22.6	49.6	22.6	22.9
62	22.6	49.6	22.6	22.9
63	23.2	45.3	22.4	22.9
64	23.4	49.8	23.4	23.8
65	23.3	50.6	23.6	24
66	23.3	51	23.8	24.1
67	23.4	51.1	24	24.4
68	23.9	51.3	24	24.9
69	23.7	52.5	24.2	24.5
70	23.5	52.7	24.3	24.7
71	23.5	52.8	24.6	24.8
72	23.5	52.9	24.6	25
73	23.8	52.6	23.7	24.7
74	23.6	53.9	23.8	24.3
75	23.3	54.2	23.8	24.2
76	23.3	54.4	24.1	24.5
77	23.4	54.2	24.2	24.5
78	22.1	53.7	23.4	29.7
79	21.1	50.3	19.5	20.0
80	21.3	52	19.7	20.0
81	21.2	52.9	19.9	20.1
82	20.8	53.3	20	20.4
83	20	51.4	19.4	19.5
84	20.1	52.4	19.7	19.8
85	20.5	50.4	19.5	21.4
86	20.5	52	19.2	19.5

Table 4.20: Temperatures in two phase flow tests.

test	T_{amb} [$^{\circ}C$]	T_{air} [$^{\circ}C$]	T_{probe} [$^{\circ}C$]	$T_{venturi}$ [$^{\circ}C$]
87	20.4	50.3	19.1	19.1
88	23.9	55.5	24.3	24.9
89	23.8	57.2	24.7	25.1
90	23.4	57.5	24.8	25.2
91	23.2	57	24.8	25
92	23.4	57.8	25.1	25.4
93	22.6	51.7	22.4	22.9
94	22.8	56	23.1	23.7
95	22.8	57.3	23.5	24
96	23	57.5	23.5	24.2
97	23	57.9	23.8	24.3
98	23.1	59.2	24.7	24.8
99	23.3	58.3	24.6	24.7
100	23.5	57.8	24.4	25.1
101	23.7	58	24.5	24.6
102	23.6	58.2	24.7	24.7
103	23.2	51.3	22.9	22.8
104	21.9	72.1	25.5	26.6
105	21.8	73.6	25.3	26.5
106	22	73.9	26.1	27.01
107	22.2	75.4	25.8	26.8
108	22.8	72	25.5	26.3
109	22.8	76.2	26.2	27.3
110	23	75.8	26.5	27.4

Table 4.21: Temperatures in two phase flow tests.

test	pressure [bar]	$\Delta p_{in-gola}$ [mbar]	$\Delta p_{irr,in-out}$ [mbar]
1	0.038	3.617	3.701
2	0.038	4.030	4.326
3	0.039	4.857	5.263
4	0.091	11.152	8.077
5	0.092	11.244	8.077
6	0.091	11.290	8.702
7	0.092	11.428	8.702
8	0.092	11.795	9.639
9	0.092	11.795	9.639
10	0.092	12.025	9.952
11	0.092	11.933	10.265
12	0.092	12.025	10.265
13	0.092	12.485	10.890
14	0.095	12.760	11.202
15	0.095	13.220	11.827
16	0.096	13.495	12.140
17	0.095	12.163	9.952
18	0.095	11.612	8.389
19	0.096	13.725	12.140
20	0.091	11.612	9.640
21	0.091	12.714	11.515
22	0.091	11.841	9.640
23	0.091	11.290	8.702
24	0.091	11.565	9.327
25	0.091	11.979	10.265
26	0.091	12.62	11.202
27	0.092	13.128	11.823
28	0.090	11.152	8.389
29	0.090	11.474	9.326
30	0.091	12.393	10.990
31	0.091	11.841	9.952
32	0.092	12.898	11.827
33	0.106	15.334	13.390
34	0.105	14.828	12.765
35	0.105	14.139	11.828
36	0.104	13.357	10.577
37	0.103	13.036	9.639
38	0.106	15.333	13.390
39	0.105	14.690	12.452
40	0.105	14.231	11.827
41	0.104	13.403	10.577
42	0.103	13.082	9.640
43	0.112	14.185	10.577

Table 4.22: Differential pressure in two phase flow tests.

test	<i>pressure</i> [bar]	$\Delta p_{in-gola}$ [mbar]	$\Delta p_{irr,in-out}$ [mbar]
44	0.112	14.690	11.515
45	0.112	15.425	12.765
46	0.113	15.977	13.390
47	0.113	16.482	14.328
48	0.118	14.966	10.890
49	0.119	15.747	12.140
50	0.119	16.298	13.078
51	0.119	17.125	14.328
52	0.120	17.585	14.953
53	0.127	16.390	12.140
54	0.127	16.896	12.765
55	0.127	17.538	14.015
56	0.127	18.182	14.953
57	0.128	18.641	15.890
58	0.125	16.023	11.827
59	0.125	16.666	12.765
60	0.126	17.447	14.015
61	0.127	18.274	15.265
62	0.127	18.642	15.891
63	0.134	17.493	12.452
64	0.133	18.090	13.703
65	0.134	18.87	15.266
66	0.134	19.285	15.891
67	0.135	19.836	16.828
68	0.140	18.366	13.078
69	0.140	18.963	14.328
70	0.141	19.974	15.578
71	0.142	20.480	16.516
72	0.142	21.031	17.454
73	0.148	19.652	13.703
74	0.148	20.158	14.953
75	0.149	21.031	16.516
76	0.150	21.812	17.766
77	0.151	22.455	18.704
78	0.166	21.628	14.953
79	0.166	21.950	15.891
80	0.166	22.686	16.516
81	0.167	22.915	17.141
82	0.167	23.466	18.079
83	0.168	24.155	19.330
84	0.169	25.166	20.892
85	0.170	22.317	15.578
86	0.171	23.742	17.767

Table 4.23: Differential pressure in two phase flow tests.

test	pressure [bar]	$\Delta p_{in-gola}$ [mbar]	$\Delta p_{irr,in-out}$ [mbar]
87	0.174	26.040	21.517
88	0.164	22.547	15.578
89	0.165	22.685	16.828
90	0.166	23.742	18.391
91	0.167	24.385	19.642
92	0.167	24.982	20.580
93	0.165	21.766	15.578
94	0.164	22.639	16.828
95	0.167	24.845	20.580
96	0.165	23.098	17.766
97	0.167	24.155	19.642
98	0.166	24.845	20.579
99	0.165	24.017	19.329
100	0.162	21.720	15.265
101	0.163	22.501	16.516
102	0.164	23.236	18.080
103	0.170	25.304	20.891
104	0.255	35.504	24.330
105	0.255	35.872	26.831
106	0.252	35.045	24.017
107	0.258	38.721	33.395
108	0.259	37.526	30.581
109	0.258	38.353	32.769
110	0.253	35.734	26.831

Table 4.24: Differential pressure in two phase flow tests.

At the end of each run the volumetric void fraction is measured (5-10 times to have a sufficient statistics) through the quick closing valves (QCV). This method allows to measure the average void fraction in the whole volume of the test section, i.e. the mean value between the void fraction in the first part of the test section (where annular wavy flow pattern occurs), the one downstream the VFM (where dispersed flow was seen) and the one inside the VFM. The measured void fraction has been compared with the predictions of the Chisholm slip model (section 2.5) and showed a very good agreement.

4.3.1 Analysis of VFM two-phase behaviour

The behavior of the VFM in its two-phase operation is described by the signals associated to the two differential pressure Δp_v between the inlet section and the minimum section (throat) and the Δp_{irr} irreversible differential pressure between the upstream and downstream of the Venturi.

In Fig. 4.15 and 4.16 Δp_v and Δp_{irr} are shown as a function of the total flow rate.

Figure 4.16 reports the irreversible pressure drop between the VFM inlet and outlet, versus the total flow rate. Since this pressure drop is very small, a great accuracy of the transducer is necessary. The previous experimental campaigns showed that the dependency of the irreversible pressure loss on the superficial velocity of the phases and on the density of the gas phase is influenced by the flow pattern; the best-fit of the present experimental campaign allowed the development of the equations 4.13 and 4.14 for wavy-stratified and dispersed-annular flow patterns.

Instead, in Fig. 4.17 and 4.18 Δp_v and Δp_{irr} are shown as a function of the gas superficial velocity.

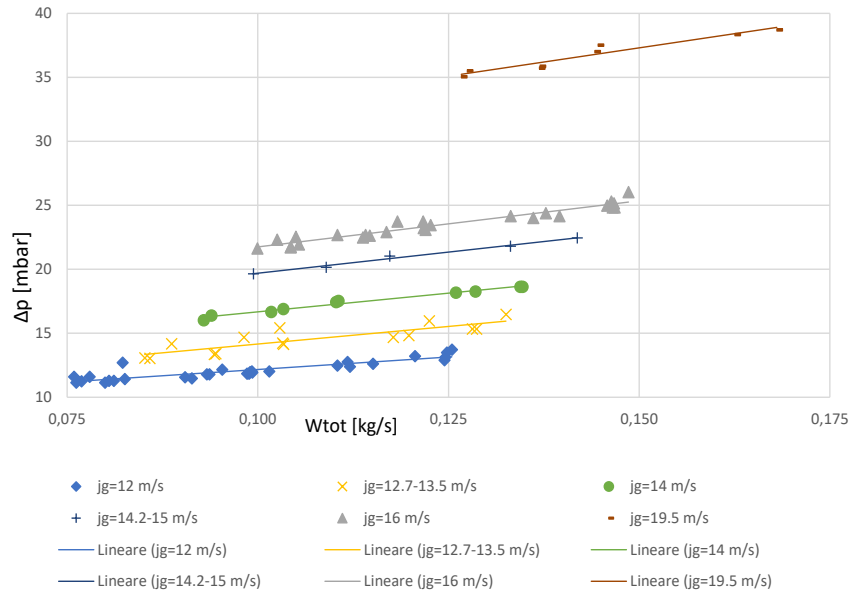


Figure 4.15: Two-phase inlet-throat pressure drops in VFM vs total flow rate.

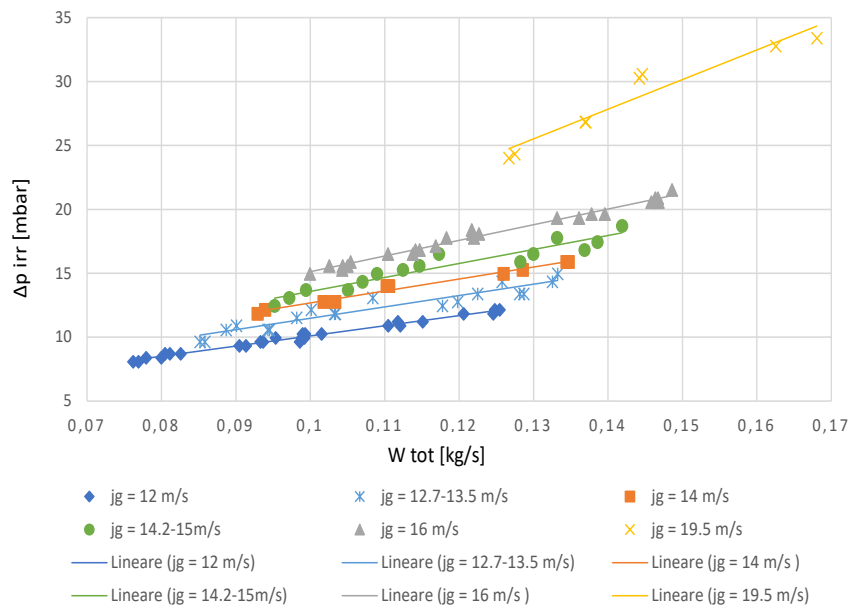


Figure 4.16: Two-phase irreversible pressure drops in VFM vs total flow rate.

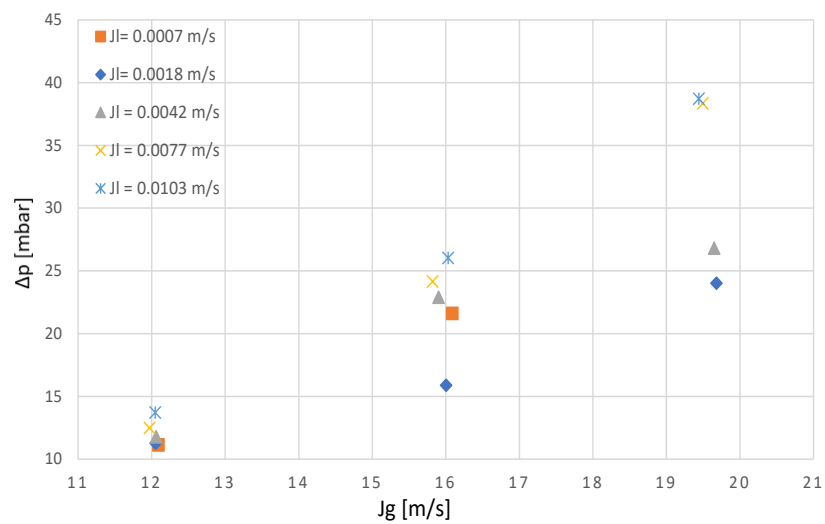


Figure 4.17: Two-phase inlet-throat pressure drops in VFM vs superficial velocity of the two phases.

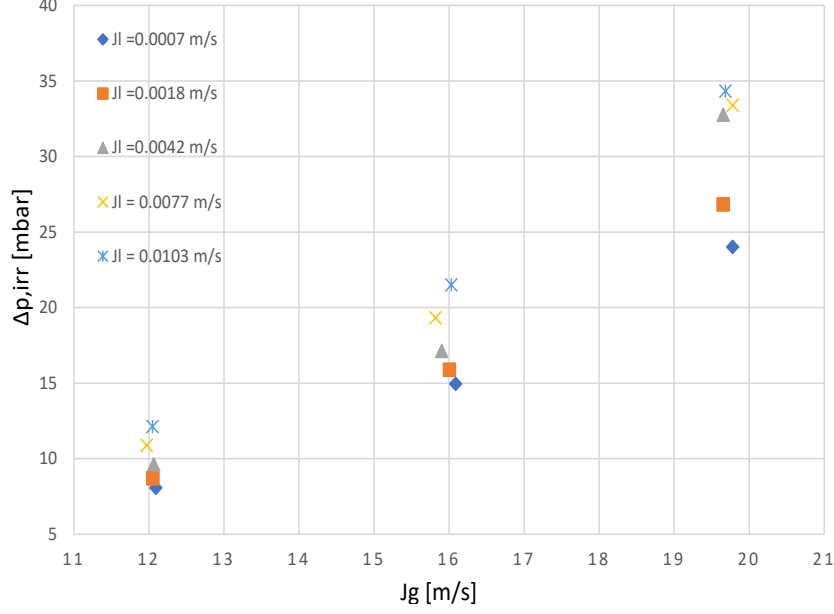


Figure 4.18: Two-phase irreversible pressure drops in VFM vs superficial velocity of the two phases.

Using the approach based on the work of Lockhart and Martinelli, the total mass flow rate in the VFM can be estimated as:

$$W_{tot} = K_g \sqrt{2 \Delta p_g \Phi_g^2 \rho_g} \quad (4.10)$$

where K_g relate to gas phase, Δp_g is the pressure drop of the gas phase estimated from the superficial velocity of the gas and from the discharge coefficient of VFM, Φ_g^2 is the two-phase flow multiplier that considers the effect of the gas phase and ρ_g is the gas density. On the ground of the previous campaigns, the two phase flow multiplier is expressed as a function of the Martinelli parameter χ (figure 4.19):

$$\phi_g^2 = \frac{\Delta p_{TP}}{\Delta p_g} = 8.3791 \chi + 1.002 \quad (4.11)$$

where χ is calculated as:

$$\chi = \frac{(1-x)}{x} \left(\frac{\rho_g}{\rho_l} \right)^2 \quad (4.12)$$

with x flow quality and the two constants were obtained as best-fit of the present campaign.

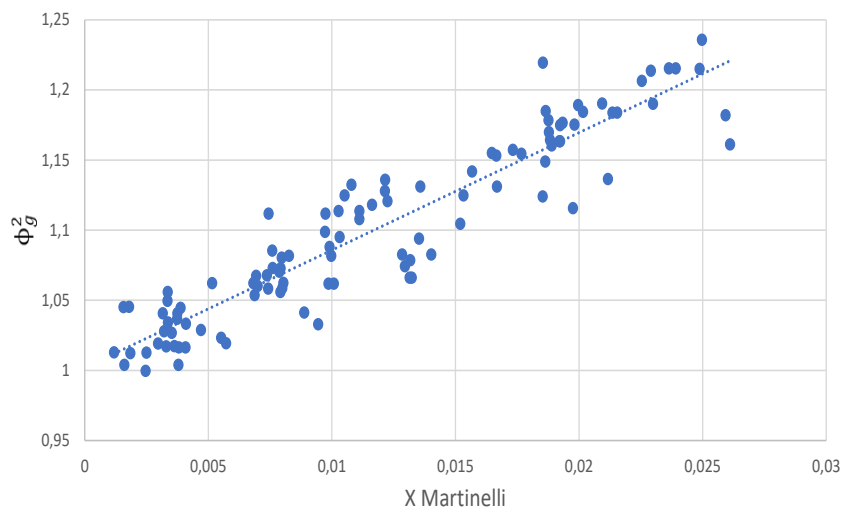


Figure 4.19: Two-phase multiplier as a function of Martinelli parameter.

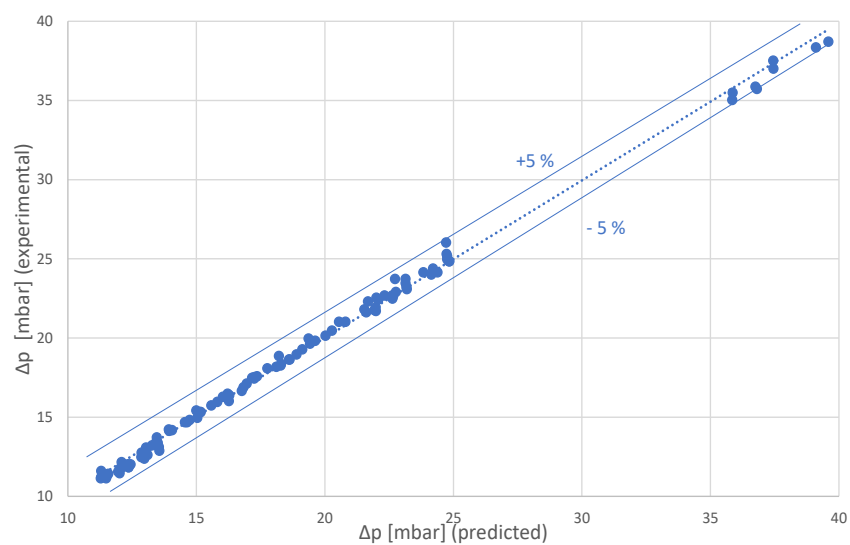


Figure 4.20: VFM pressures drop: experimental data vs. predicted values [eq.4.11].

In Fig. 4.20 the pressure drops evaluated with the new correlation are compared with the experimental values, showing a very good agreement and

a calculation accuracy better than 5%.

Instead, analysing the irreversible pressure losses is highlighted the effect of the liquid phase and, based on the old campaign, it is found the dependency of the irreversible pressure loss on the superficial velocity of the phases and on the density of the gas phase:

$$\Delta P_{irr} = 0.2205(\rho_g J_g^{1.91}) \left(\frac{J_l}{J_g} \right)^{0.137} \quad (4.13)$$

$$\Delta P_{irr} = 0.2405(\rho_g J_g^{1.903}) \left(\frac{J_l}{J_g} \right)^{0.147} \quad (4.14)$$

where equation 4.13 is for wavy stratified flow pattern and equation 4.14 for dispersed annular flow pattern.

The discrepancy between the prediction obtained from the previous equations and the experimental data is approximately 10%, while 12% discrepancy was found in the previous studies which did not considered the different flow patterns. Therefore, the knowledge of the reversible and irreversible pressure drop through the VFM could allow the evaluation of the superficial velocities of the two phases and therefore the total two-phase flow rate, but the identification of the flow pattern is fundamental in order to properly correlate the irreversible pressure drop and the two-phase multiplier to the phases superficial velocities.

4.3.2 Analysis of SIET ECP two-phase behavior

The flow is created by imposing the flow rates of the two phases at the entrance of the test section.

The relationship between the capacitance and the void fraction depends on the dielectric values of the two phases, on the surfaces of the sensors, on the separation distance between the two electrodes and on the voltage distribution inside the measurement volume, that depends on the phase distribution. The different distribution of the phases in the two conditions is clearly identified by the ECP probe.

In the tests at low air flow rates, the realized flow is stratified wavy, with negligible liquid flow entrained in the gaseous core.

Instead, at higher air flow rates the flow pattern tends to annular. In the annular flow the measurements taken from the external electrodes are not very sensitive to the core region flow, because the preferential path of the electric field lines is located in the continuous liquid film; so it is necessary to take into account signals of the central electrode.

The curves in figures below show the normalized signals $V_{i,j}^*$ as a function of the position of the electrodes parameterized with the experimental value of the void fraction calculated with the QVC. $V_{i,j}^*$ is calculated as follows:

$$V_{i,j}^* = \frac{RMS_{TP-ij} - RMS_{l-ij}}{RMS_{g-ij} - RMS_{l-ij}} \quad (4.15)$$

where the subscript ij identifies the measuring electrodes combination and RMS is the root mean square of electrical signals. This value is a function of local void fraction and sensitivity of the probe. The results obtained are in accordance with all those of previous campaigns with a wider range of water flow (0-190 l/h).

Increasing the air flow rate, a change in the flow pattern is observed: wavy stratified, dispersed-annular and annular. This different distribution of the phases is clearly identified by the ECP probe from very high signals values to very low signal values (Fig. 4.21,4.22,4.23 and 4.25,4.26,4.27).

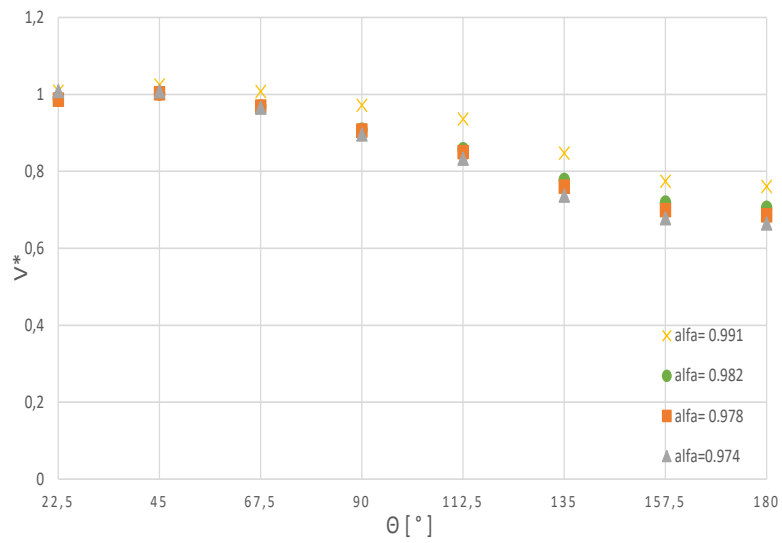


Figure 4.21: Dimensionless voltage drop electrode 1 (top) $Wg = 0.07 \text{ kg/s}$.

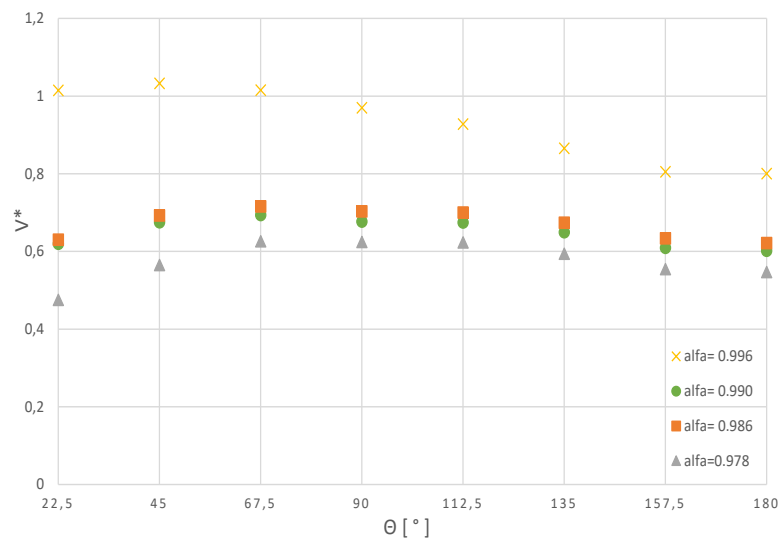


Figure 4.22: Dimensionless voltage drop electrode 1 (top) $Wg = 0.09 \text{ kg/s}$.

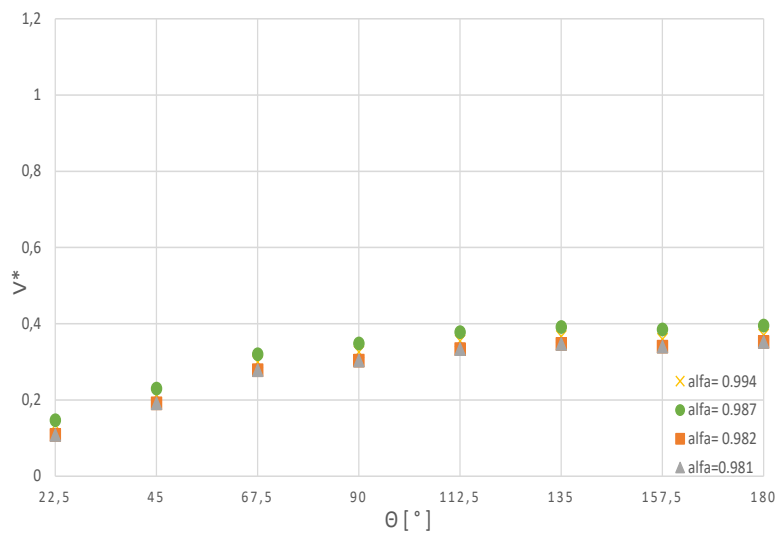


Figure 4.23: Dimensionless voltage drop electrode 1 (top) $Wg = 0.12kg/s$.

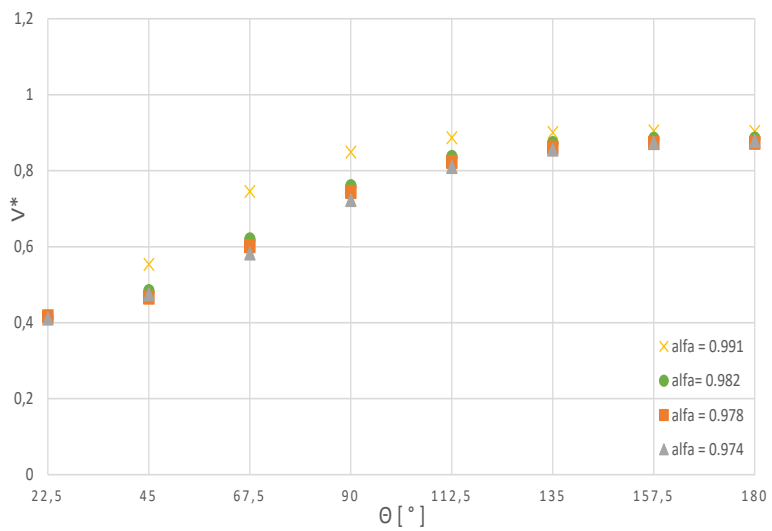


Figure 4.24: Dimensionless voltage drop electrode 9 (bottom) $Wg = 0.07kg/s$.

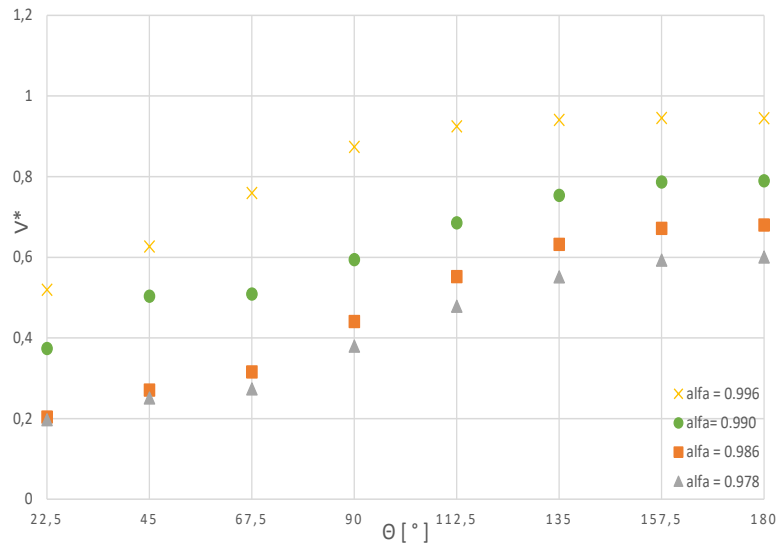


Figure 4.25: Dimensionless voltage drop electrode 9 (bottom) $Wg = 0.09 \text{ kg/s}$.

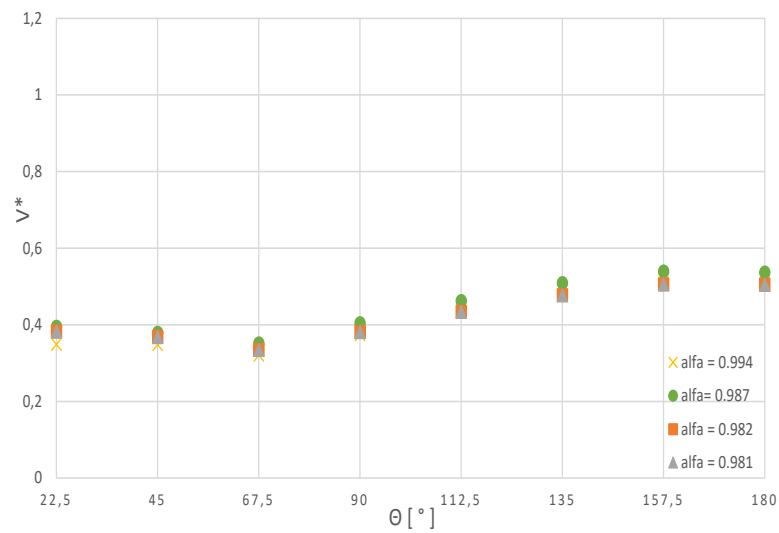


Figure 4.26: Dimensionless voltage drop electrode 9 (bottom) $Wg = 0.12 \text{ kg/s}$.

In the case of annular flow, the measurements taken from the external

electrodes are rather insensitive to the void fraction (Fig. 4.23 and 4.26) , so it is necessary to consider the measurements of the central electrode. Figure 4.27 shows that the signal increases linearly with the void fraction, the trend of the curves depends on the position of the electrodes respect to the vertical axis of the tube.

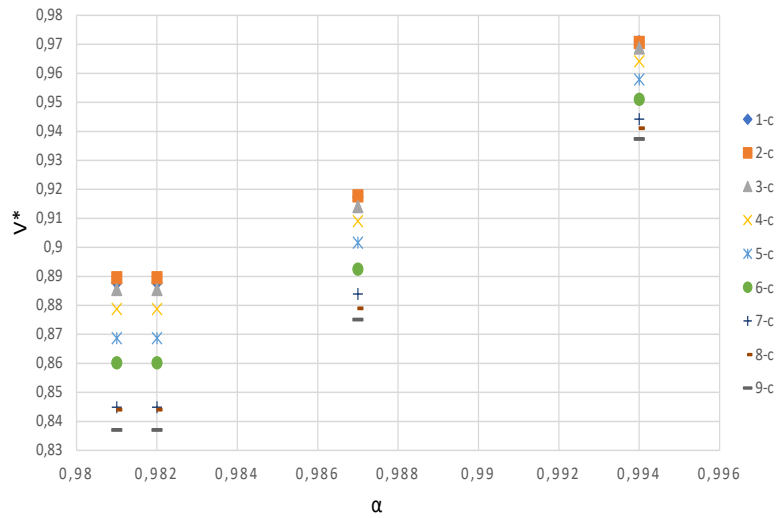


Figure 4.27: Dimensionless voltage drop associated with the measurements of the central electrode vs experimental void fraction $Wg = 0.12kg/s$.

All these results are in accordance with those obtained from the DENERG ECP made with concave electrodes (section 4.3.3).

4.3.3 Analysis of the new DENERG ECP two-phase behavior

To evaluate the dynamic behaviour of the concave sensors (configuration A and B) Fig. 4.28 and 4.29 show the dependency between the measured capacitance and the superficial velocity of the liquid phase, parameterized with the superficial velocity of the gas phase. The analysis of the signals shows that the measured capacitance increases as the void fraction increase. In particular, their sensitivity is good in case of dispersed-annular flow pattern (high capacitance values), whereas the sensitivity is poorer for the stratified-wavy flow pattern. In particular the probe A, which has a bigger surface, shows a steeper increase of the capacitance when the air superficial velocity increases; the capacitance reaches the full scale value of the measuring instrument (4 pF) for high values of the air superficial velocity (greater than 16 m/s); in this case, an ECP with lower surface (probe B) is necessary.

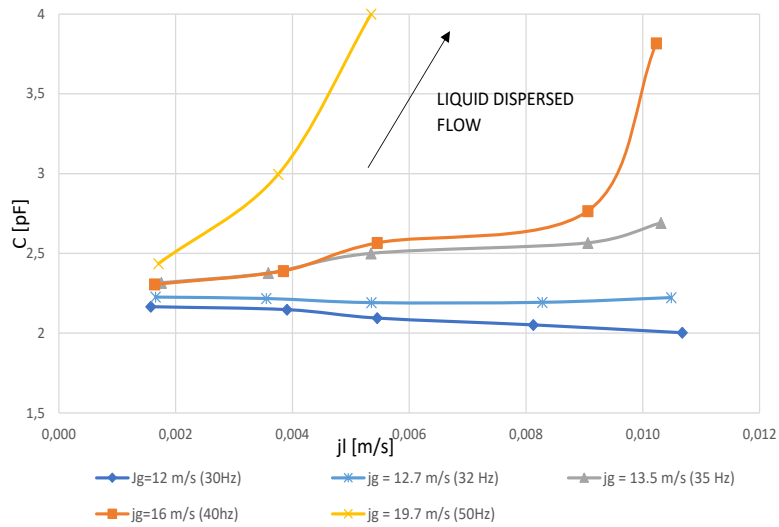


Figure 4.28: Capacitance values vs liquid superficial velocity, parameterized with gas superficial velocity (Electrodes A).

In the case of the second configuration of the concave electrodes all the range of the liquid flow rate and air flow rate is analyzed. The relationship between the capacitance measured with the probe B and the void fraction measured by the QCV method has also been studied in the whole ranges of air and water superficial velocities.

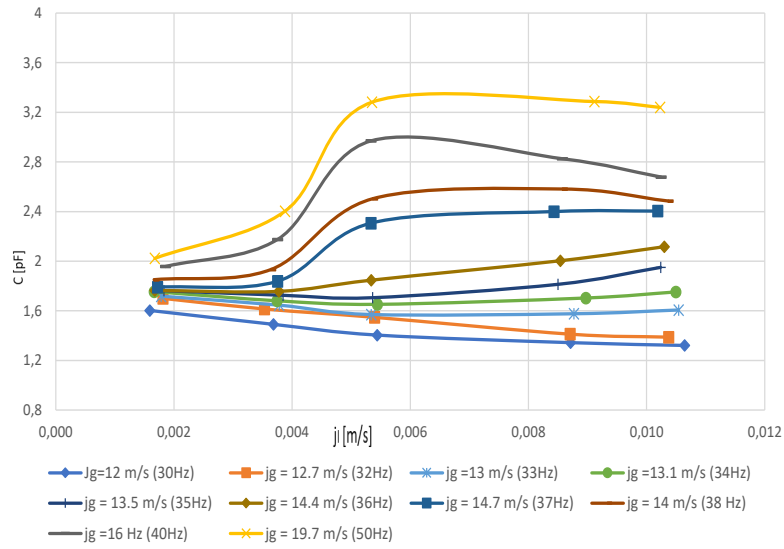


Figure 4.29: Capacitance values vs liquid superficial velocity, parameterized with gas superficial velocity (Electrodes B).

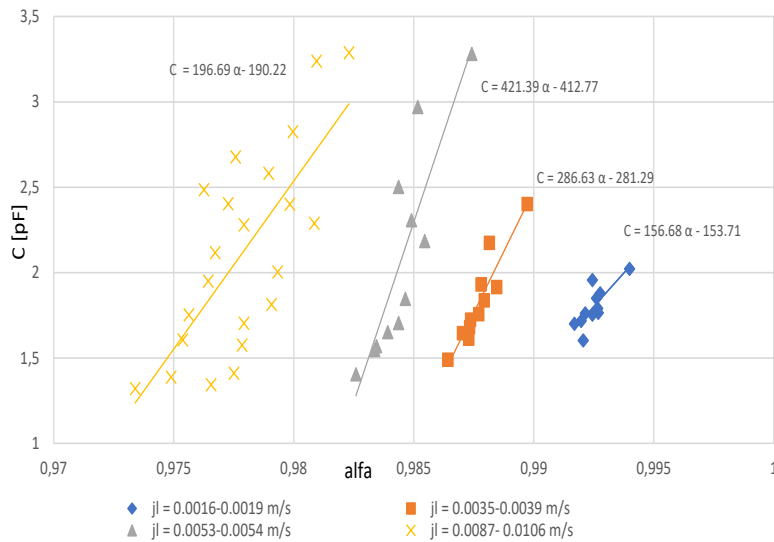


Figure 4.30: Capacitance values vs experimental void fraction (four different range of water superficial velocities).

In figure 4.30 the results have been grouped on the basis of the water superficial velocities, four ranges of water superficial velocity have been considered and for each of them a different best-fit line has been found. Moving from the left towards the right of the void fraction axis, the flow patterns changes from wavy stratified to dispersed annular flow. Therefore the capacitance signal is not sufficient to determine the void fraction. The knowledge of the flow pattern is also necessary.

4.4 Combining signals: a general outline

The final goal is to combine the signals of the instruments to get the flow rate without the needing of the visual observation such as in the case of an opaque case. The general outline to follow:

1. *Identification of the flow pattern*

The elaboration of the signals from the SIET ECP provide information on the flow pattern:

- case A) wavy stratified
- case B) dispersed annular

2. *Average void fraction*

Through the value of capacitance elaborated from the DENERG ECP' signals, having identified the flow pattern, I obtain the average void fraction.

3. *Guess flow quality*

I introduce an iterative method, assuming x_{guess} . The parameter of comparison for convergence is represented by the irreversible pressure drops (point 8).

4. *Two-phase flow multiplier*

On the basis of the best fit' results of the present campaign the following correlation of the two-phase flow multiplier, function of the Martinelli parameter, has been developed:

$$\phi_g^2 = 8.3791\chi_{Martinelli} + 1.002 \quad (4.16)$$

where χ is calculated as

$$\chi_{Martinelli} = \frac{(1-x)}{x} \left(\frac{\rho_g}{\rho_l} \right)^2 \quad (4.17)$$

5. *Pressure drop of the gas phase*

Estimated from the signals of differential pressure between the inlet section and the minimum section and the two-phase multiplier:

$$\Delta p_g = \frac{\Delta p_v}{\phi_g^2} \quad (4.18)$$

6. *Volumetric gas flow rate*

I obtain the volumetric gas flow rate and all the quantities correlated:

$$Q = C_d \cdot A_{min} \cdot \left(\frac{2 \cdot \Delta p}{\rho \cdot (1 - \beta)^4} \right)^{0.5}, \quad (4.19)$$

$$W_g = Q_g \cdot \rho_g, W = \frac{W_g}{x}, W_l = W \cdot (1 - x) \quad (4.20)$$

so:

$$j_g = \frac{W_g}{A \cdot \rho_g}, j_l = \frac{W_l}{A \cdot \rho_l} \quad (4.21)$$

7. *Irreversible pressure drops*

The best fit of the present experimental campaign allowed the development of the following equations:

$$\Delta P_{irr} = 0.2205(\rho_g J_g^{1.91}) \left(\frac{J_l}{J_g} \right)^{0.137} \quad (4.22)$$

$$\Delta P_{irr} = 0.2405(\rho_g J_g^{1.903}) \left(\frac{J_l}{J_g} \right)^{0.147} \quad (4.23)$$

where equation 4.22 is for wavy stratified flow pattern and equation 4.23 for dispersed annular flow pattern.

8. *Comparison*

I compare the value of the irreversible pressure drop from VFM's signal to the value of the irreversible pressure drop obtained from the equation (point 7).

Chapter 5

Conclusions and perspectives

In this study a spool piece constituted by a Venturi Flow Meter (VFM), a new Electric Capacitance Probe with concave electrodes designed at DENERG-Politecnico of Torino (DENERG ECP) and the electrical capacitance probe designed by SIET (SIET ECP) have been characterized for wavy stratified and dispersed-annular flow pattern.

The results of the SIET ECP agree with those of the previous experimental campaigns. The elaboration of the signals from the SIET ECP can provide information on the flow pattern.

The DENERG ECP and the VFM demonstrated the possibility to determine respectively the average void fraction and the superficial velocity of the phases once the flow pattern is known.

The information from the SIET ECP and DENERG ECP can be combined; a theoretical procedure has been developed in order to evaluate the air and water flow rates, and therefore the total two-phase flow rate.

In the future, taking the present experimental results into account, the design modification of the DENERG ECP will improve the performance of this probe; a second probe will also be positioned downstream the VFM and the range of the flow patterns will be extended.

The final goal is the development of a two-phase flow forecasting model based on the transducers responses.

List of Figures

2.1	Schematic representation of horizontal flow regimes [6].	11
2.2	Taitel and Duckler's map for horizontal tubes [9].	15
2.3	Classical Venturi Flow Meter [14]	20
2.4	Venturi flow meter types [14].	21
2.5	Permanent pressure drop in differential flow meter [14].	21
2.6	Scheme of ring and concave type sensor [16].	25
3.1	Picture of the experimental facility	30
3.2	Schematic of experimental facility	31
3.3	Picture of the National Instrument DAQ system and Analog Device-Evolution board AD7746.	34
3.4	Evolution Software v2.2 [18].	34
3.5	Technical design of VFM.	36
3.6	Picture of VFM	37
3.7	Calibration monophasic with air of VFM [11].	38
3.8	Experimental monophasic discharge coefficient for VFM [11].	38
3.9	Picture of the probe.	39
3.10	Position of the electrodes in the probe.	40
3.11	Schematic of the probe electronic [19].	40
3.12	Numerical codes that identify electrodes.	42
3.13	Picture of concave electrodes' sensor.	43
3.14	Schematic of the concave electrodes' sensor. [2]	44
4.1	Calibration curve for the evaluation of the air mass flow.	47
4.2	Differential pressure measured in the orifice and in VFM vary- ing the frequency.	48
4.3	Temperature along the test section versus air superficial velocity- single-phase.	49
4.4	Temperature along the test section versus air superficial velocity- two-phase.	49
4.5	RMS values function of the angular distance, case with air.	50

4.6	RMS values function of the angular distance, case with water.	51
4.7	RMS values function of the angular distance (exciting electrode 1).	52
4.8	RMS values function of the angular distance (exciting electrode 9.)	53
4.9	alpha trend as a function of the level.	55
4.10	Signals (electrode exciting: 1, receiving electrodes 2:9) function of the angle for different levels of water of the circuit.	56
4.11	Signals (electrode exciting: 9, receiving electrodes 1:8) function of the angle for different levels of water of the circuit.	57
4.12	Calibration of the configuration A of the concave electrodes' sensor.	58
4.13	Calibration of the configuration B of the concave electrodes' sensor.	59
4.14	Data of the experimental campaign in Taitel and Duckler's map.	60
4.15	Two-phase inlet-throat pressure drops in VFM vs total flow rate.	76
4.16	Two-phase irreversible pressure drops in VFM vs total flow rate.	77
4.17	Two-phase inlet-throat pressure drops in VFM vs superficial velocity of the two phases.	77
4.18	Two-phase irreversible pressure drops in VFM vs superficial velocity of the two phases.	78
4.19	Two-phase multiplier as a function of Martinelli parameter.	79
4.20	VFM pressures drop: experimental data vs. predicted values [eq.4.11].	79
4.21	Dimensionless voltage drop electrode 1 (top) $Wg = 0.07kg/s$.	82
4.22	Dimensionless voltage drop electrode 1 (top) $Wg = 0.09kg/s$.	82
4.23	Dimensionless voltage drop electrode 1 (top) $Wg = 0.12kg/s$.	83
4.24	Dimensionless voltage drop electrode 9 (bottom) $Wg = 0.07kg/s$.	83
4.25	Dimensionless voltage drop electrode 9 (bottom) $Wg = 0.09kg/s$.	84
4.26	Dimensionless voltage drop electrode 9 (bottom) $Wg = 0.12kg/s$.	84
4.27	Dimensionless voltage drop associated with the measurements of the central electrode vs experimental void fraction $Wg = 0.12kg/s$.	85
4.28	Capacitance values vs liquid superficial velocity, parameterized with gas superficial velocity (Electrodes A).	86
4.29	Capacitance values vs liquid superficial velocity, parameterized with gas superficial velocity (Electrodes B).	87
4.30	Capacitance values vs experimental void fraction (four different range of water superficial velocities).	87

List of Tables

3.1	Experimental matrix.	26
3.2	Typical test run.	27
3.3	Models and range of transducers.	32
3.4	Conversion laws of the signals from volt into physical quantities.	33
3.5	Parameters of the VFM.	35
3.6	Parameters of concave electrodes.	44
4.1	Parameters of the VFM	45
4.2	Parameters of the orifice	46
4.3	Temperatures evaluated during single-phase tests with only air.	46
4.4	Differential pressure drops evaluated during single-phase tests with only air.	46
4.5	Air mass flow rate varying the frequency.	47
4.6	Polynomial coefficients of best fit (4-degree) case single-phase with air.	51
4.7	Polynomial coefficients of best fit (4-degree) case single-phase with demineralized water.	51
4.8	ECP probe: static test conditions.	54
4.9	Parameters of concave electrodes.	58
4.10	Experimental matrix in two phase flow tests with $f_{inverter} = 20Hz$	62
4.11	Experimental matrix in two phase flow tests with $f_{inverter} = 30Hz$	63
4.12	Experimental matrix in two phase flow tests with $f_{inverter} = 30Hz$	64
4.13	Experimental matrix in two phase flow tests with $f_{inverter}$ from 32 to 38 Hz.	65
4.14	Experimental matrix in two phase flow tests with $f_{inverter}$ from 32 to 38 Hz.	66
4.15	Experimental matrix in two phase flow tests with $f_{inverter} = 40 Hz$	67

4.16	Input datas in two phase flow tests with $f_{inverter} = 40Hz$	68
4.17	Experimental matrix in two phase flow tests with $f_{inverter} = 50Hz$	69
4.18	Experimental matrix in two phase flow tests with $f_{inverter} = 50Hz$	69
4.19	Temperatures in two phase flow tests.	70
4.20	Temperatures in two phase flow tests.	71
4.21	Temperatures in two phase flow tests.	72
4.22	Differential pressure in two phase flow tests.	73
4.23	Differential pressure in two phase flow tests.	74
4.24	Differential pressure in two phase flow tests.	75

Bibliography

- [1] Mamoru Ishi, Takashi Hibiki, *Thermo-fluid dynamics of two-phase flow*, Springer 2011.
- [2] Wael H. Ahmed and Basel I. Ismail, *Innovative techniques for two-phase flow measurements* from Recent Patents on Electrical Engineering 2008, 2007.
- [3] Lowe DC, Rezkallah KS., *A capacitance sensor for the characterization of microgravity two-phase liquid-gas flows* from Meas Sci Technol, 1999, pp 965-975.
- [4] G. Monni, M. De Salve M, B. Panella, *Prog. Nucl. Energy* 77 167-175, 2014.
- [5] A.J. Ghajar *Non-boiling heat transfer in gas-liquid flow in pipes - a tutorial*, 2005.
- [6] Collier J G and Thome J R, *Convective Boiling and Condensation*, Oxford science publications, 3th edition, 1996.
- [7] J. Thome, *Engineering Data Book III*, Wolverine Tube INC., 2004.
- [8] G. Monni, *Special instrumentation for two-phase flow*, Tesi di Dottorato, Dipartimento Energia, Politecnico di Torino (2013).
- [9] Noé Pinto del Corral, *Analysis of two-phase flow pattern maps*, Brno University of Technology, 2014.
- [10] D. Chisholm, D. H. Rooney *Research note: Two-phase flow through sharp-edged orifices*, J. Mech Eng. Sci 16 353-55, 1974.
- [11] M. Caramello, M. De Salve, G. Monni, B. Panella, *Modellizzazione di uno spool piece per la stima dei parametri caratteristici dei deflussi bifase*, 2014.

- [12] *Measurement of two-phase flow parameters*, Academic Press, 1978.
- [13] R. Steven *Horizontally installed differential pressure water wet gas flow performance review*, In: north sea flow measurement workshop, 2006.
- [14] www.engineeringToolBox.com
- [15] C.R. Baker, *Flow measurement handbook*, Cambridge University Press, 2000.
- [16] Ahmed and Ismail, *Innovative Techniques for two-phase flow measurements*, Patents on Electrical Engineering (2007).
- [17] Analog Devices, 24-bit Capacitance-to-digital Converter with Temperature Sensor AD7746.
- [18] Analog Devices, AD7746 Evolution Board data sheet.
- [19] M.De Salve, G.Monni, B.Panella, C.Randaccio *Electrical capacitance probe characterisation for vertical annular air-water flow investigation*, 2012.
- [20] G.Monni, M.Caramello, M.De Salve, B.Panella *Messa a punto di una metodologia deterministica/statistica per l'analisi dei segnali dello spool piece venturi/sonda ad imoedenza*, ReportRDS/PAR 2014.